

# Satellite-based Near-Real-Time Global Daily Terrestrial Evapotranspiration Estimates

Lei Huang<sup>1\*</sup>, Yong Luo<sup>1\*</sup>, Jing M. Chen<sup>2,3</sup>, Qihong Tang<sup>4,5</sup>, Tammo Steenhuis<sup>6</sup>, Wei Cheng<sup>7</sup> and Wen Shi<sup>1</sup>

<sup>1</sup>Department of Earth System Science, Ministry of Education Key Laboratory for Earth System Modeling, Institute for Global Change Studies, Tsinghua University, Beijing 100084, China

<sup>2</sup>Key Laboratory for Humid Subtropical Ecogeographical Processes of the Ministry of Education, School of Geographical Sciences, Fujian Normal University, Fuzhou, 350007, China

<sup>3</sup>Department of Geography and Planning, University of Toronto, Ontario, M5S 3G3, ON, Canada

<sup>4</sup>Key Laboratory of Water Cycle and Related Land Surface Processes, Institute of Geographic Sciences and Natural Resources Research, Chinese Academy of Sciences, Beijing 100101, China

<sup>5</sup>University of Chinese Academy of Sciences, Beijing 101408, China

<sup>6</sup>Department of Biological and Environmental Engineering, Cornell University, Ithaca 14850, New York, USA

<sup>7</sup>Key Laboratory of Land Surface Pattern and Simulation, Institute of Geographic Sciences and Natural Resources Research, Chinese Academy of Sciences, Beijing 100101, China

*Correspondence to* Lei Huang (leihuang007@mail.tsinghua.edu.cn) or  
Yong Luo (Yongluo@mail.tsinghua.edu.cn)

## Abstract.

Accurate and timely information on global terrestrial actual evapotranspiration (ET) is crucial in agriculture, water resource management and drought forecasting in a changing climate. While numerous satellite-based ET products have been developed in recent decades, few provide near-real-time global terrestrial ET estimates. The MOD16 ET dataset, currently updating at the fastest rate, still experiences a delay of over two weeks. This is because most satellite-based ET algorithms rely on meteorological data from land surface models or in situ measurements, which cannot be obtained in near-real-time, resulting in delays of more than two weeks. To expedite global ET data access, we developed the Moderate Resolution Imaging Spectroradiometer (MODIS) based Variation of Standard Evapotranspiration Algorithm (VISEA) to provide global daily ET data within a week of the actual measurements at a spatial resolution of 0.05°. The VISEA model incorporates several key components: (1) A vegetation index (VI)-temperature (Ts) triangle method to simulate air temperature (Ta), serves as a basis for calculating other meteorological parameters (e.g., water vapor deficit and wind speed); (2) A daily evaporation fraction (EF) method based on the decoupling parameter, converts satellite-based instantaneous observations into daily ET estimates; (3) A net radiation calculation program takes into account cloud coverage in the atmosphere's downward longwave radiation. The VISEA model is driven by shortwave radiation from the European Centre for Medium-range Weather Forecasts (ERA5-Land) and MODIS land products, e.g., surface reflectance, land surface temperature/emissivity, land cover products, vegetation indices, and albedo as inputs. To assess its accuracy, we compared VISEA with measurements from 149 flux towers, five other satellite-based global ET products, and precipitation data from the Global Precipitation Climatology Centre (GPCC). The evaluations show that the near-real-time ET using VISEA performs with similar accuracy to other existing data products and offers a significantly shorter time frame for daily data availability. Over 12 landcover types, the mean R is about 0.6 with an RMSE of 1.4 mm day<sup>-1</sup> at a daily scale. Furthermore, the consistent spatial patterns of multi-year average

45 VISEA align closely with GPCP precipitation data, reaffirming the dataset's ability to accurately  
46 represent global terrestrial ET distribution. To emphasize the capabilities of the VISEA for drought  
47 monitoring, we analyzed the spatial and temporal variations of ET during a drought event and subsequent  
48 recovery with precipitation in the Yangtze River basin from August 26<sup>th</sup> to September 2<sup>nd</sup>, 2022. The  
49 VISEA distinctly illustrated low mean ET levels ( $<0.5 \text{ mm day}^{-1}$ ) across the Yangtze River Basin on  
50 August 28<sup>th</sup>, indicating the severity of the drought. Conversely, a noticeable increase in ET ( $>1 \text{ mm day}^{-1}$ )  
51 is observed on August 30<sup>th</sup>, signifying the retreat of the drought due to precipitation. The near-real-  
52 time global daily terrestrial ET estimates could be valuable for meteorology and hydrology applications  
53 requiring real-time data, particularly in coordinating relief efforts during droughts. The VISEA code and  
54 dataset are available at <https://doi.org/10.11888/Terre.tpdc.300782> (Huang et al., 2023a).

## 55 **1 Introduction**

56 Global terrestrial evapotranspiration (ET) is a vital component of the Earth's water cycle and energy  
57 budget. It includes evaporation from the soil and water surfaces (some studies also consider evaporation  
58 from the intercepted precipitation in canopies) and plant transpiration (Zhang et al., 2021; He et al., 2022;  
59 Wang et al., 2021a). Accurate and timely estimation of ET is essential for quantitatively assessing  
60 changes in the water cycle under climate change, vigilant monitoring drought, and effectively managing  
61 and allocating water resources (Su et al., 2020; Han et al., 2021; Aschonitis et al., 2022).

62 Near-real-time ET estimation from climate models have been widely used to assess and predict ET  
63 changes in the global water cycle under different weather conditions (Copernicus Climate Change  
64 Service, 2020). While these models such as ERA5 reanalysis offer near-real-time latent heat flux (ET in  
65 energy units) with a delay of just six days, they typically feature coarser spatial resolutions, often  $0.1^\circ$  or  
66 more. This level of resolution may limit their effectiveness for detailed assessments of drought conditions  
67 and the optimization of water resource allocation. On the other hand, obtaining highly accurate, near-  
68 real-time, or real-time ET measurements through local eddy covariance or lysimeter methods can be very  
69 valuable (Awada et al., 2022), but collecting large-scale ET data using this equipment proves to be quite  
70 challenging (Barrios et al., 2015; Tang et al., 2009).

71 Satellite remote sensing-based ET estimates outperform climate model simulations by offering high  
72 spatial resolution for detailed water use analysis, near-real-time data for prompt environmental response,  
73 and global coverage for comprehensive water cycle studies. These estimates rely on direct observations,  
74 enhancing accuracy, especially where ground data are sparse, and allow for the dynamic monitoring of  
75 land and vegetation changes. This capability underscores their importance in water resource management  
76 and climate research, complementing the broader perspectives provided by climate models.

77 The selected ET products discussed in this study embody diverse and innovative algorithmic  
78 approaches that have significantly contributed to global ET estimation and gained recognition within the  
79 scientific community. The MOD16 ET dataset, developed by Mu et al. (2007, 2011), utilizes a Penman-  
80 Monteith-based approach and is driven by MODIS land cover, albedo, fractional photosynthetically  
81 active radiation, leaf area index, and daily meteorological reanalysis data from NASA's Global Modelling

82 and Assimilation Office to estimate ET. As the first satellite-based global ET product, it played a pivotal  
83 role in providing precise estimations crucial for global drought monitoring (Mu et al., 2013).

84 The AVHRR ET dataset, developed by Zhang et al. (2006, 2009), employed a modified Penman–  
85 Monteith approach over land, integrating biome-specific canopy conductance determined by NDVI, and  
86 utilized a Priestley–Taylor approach over water surfaces. These algorithms were driven by AVHRR  
87 Global Inventory Modeling and Mapping Studies (GIMMS) NDVI, daily surface meteorology data from  
88 the National Centers for Environment Prediction/National Center for Atmospheric Research  
89 (NCEP/NCAR) reanalysis, and solar radiation from NASA/GEWEX Surface Radiation Budget Release-  
90 3.0. This dataset has significantly advanced the study of the global water cycle, capitalizing on its  
91 extensive coverage and high accuracy to provide valuable insights into global hydrological processes.

92 The FLUXCOM dataset, is notable for its utilization of machine learning to integrate eddy  
93 covariance data from the global FLUXNET tower network, surface meteorological data, and remote  
94 sensing data. This approach has made a substantial contribution to resolving the evapotranspiration  
95 paradox and has cemented its status as a crucial tool widely acknowledged within the scientific  
96 community for elucidating intricate ET dynamics. (Jung et al., 2009, 2010, 2019).

97 Additionally, GLEAM, developed by Miralles et al. (2011b) and Martens et al. (2017), holds a  
98 prominent position as one of the best satellite-based ET products, known for its unparalleled accuracy  
99 and unique algorithmic approaches that have considerably advanced global ET estimation and enhanced  
100 our understanding of land surface evapotranspiration processes. Lastly, PML, developed by Zhang et al.  
101 (2019, 2022), represents the first 250-meter global coverage ET product, providing unprecedented spatial  
102 resolution for global ET estimation and contributing to our understanding of the decline in global water  
103 availability (Zhang et al., 2023b).

104 While these satellite-based global ET products provide reasonable estimations, they do not offer  
105 near-real-time ET estimates. Despite ongoing rapid updates to the MOD16 ET dataset, it still encounters  
106 delays exceeding two weeks. Additionally, AVHRR ET spans from 1983 to 2006, PML ET covers the  
107 period from 2002 to 2019, FLUXCOM data covers from 1950 to 2016, and GLEAM ET extends from  
108 2001 to 2022. Notably, the four later ET products exhibit data gaps exceeding one year, posing challenges  
109 for near-real-time estimation. Furthermore, NASA's ECOsystem Spaceborne Thermal Radiometer  
110 Experiment on Space Station (ECOSTRESS) aims to deliver global-scale ET estimation (Fisher et al.,  
111 2020). However, as of now, the data from ECOSTRESS have not been published, resulting in a lack of  
112 satellite-based global near-real-time ET estimation.

113 The Variation of the Moderate Resolution Imaging Spectroradiometer Standard Evapotranspiration  
114 Algorithm (VISEA) was introduced by Tang et al. (2009), which was designed for the near-real-time  
115 monitoring of crop consumption at the basin scale. Huang et al. (2017) examined its reliability by  
116 conducting a comprehensive assessment comparing its ET values with flux tower measurements and  
117 other gridded ET datasets across various scales in China. Subsequently, to improve the model, a  
118 decoupling parameter for daily evaporation fraction (EF) was introduced (Huang et al., 2021), and the

119 atmospheric emissivity and cloud coverage in the daily net radiation calculation was included (Huang et  
120 al., 2023b). Global terrestrial application and evaluation of the developed VISEA algorithm have not  
121 been conducted so far. In this study, we employ this VISEA algorithm along with MODIS surface  
122 reflectance (MOD09CMG) (Vermote, 2015), land surface temperature/emissivity (MOD11C1) (Wan et  
123 al., 2015), land cover products (MCD12C1) (Friedl & Sulla-Menashe, 2015), vegetation indices  
124 (MOD13C1) (Didan, 2015), albedo (MCD43C3) (Schaaf & Wang 2015), and hourly shortwave radiation  
125 from ECMWF ERA5-Land (Sabater, 2019) to provide global daily ET estimates from 2001 to 2022.

126 The performance of VISEA was evaluated with data from meteorological instruments and eddy  
127 covariance measurements at 149 flux towers of FLUXNET (Pastorello et al., 2020). We assessed the  
128 spatial distribution averages of VISEA by comparing its multi-year average with established ET datasets  
129 GLEAM (Martens et al., 2017; Miralles et al., 2011), FLUXCOM (Jung et al., 2009, 2010, 2018),  
130 AVHRR (Zhang et al., 2009, 2010), MOD16 (Mu et al., 2007, 2011), PML (Zhang et al., 2019, 2022)  
131 and precipitation data from the Global Precipitation Climatology Centre (GPCC) (Udo et al., 2011).

132

## 133 **2. Methods**

### 134 **2.1 Description of the VISEA algorithm**

135 VISEA, short for the Variation of the Moderate Resolution Imaging Spectroradiometer Standard  
136 Evapotranspiration Algorithm, is a modification of the MODIS standard Evapotranspiration (ET)  
137 algorithm. The original MODIS algorithm, created by Mu et al. (2007 and 2011), is based on the Penman-  
138 Monteith method. VISEA introduces two significant modifications. First, it employs the Vegetation (VI)-  
139 Temperature (Ts) Triangle method, originally developed by Nishida et al. (2003), to estimate air  
140 temperature. Second, VISEA incorporates hourly data on shortwave downward radiation from the ERA5-  
141 Land dataset to calculate daily average energy. These two advancements enable VISEA to estimate large-  
142 scale ET without needing local measurements as supplementary data.

143 Unlike energy budget-based ET algorithms (such as SEBS, METRIC, and Alexi), which calculate  
144 ET (latent heat flux) as the residual of the net radiation, subtracting soil heat flux and sensible heat flux.  
145 VISEA estimates ET using the Penman-Monteith equation, placing it in a different category of satellite-  
146 based global ET products currently in use. VISEA is a two-source model, which means the *ET* in one  
147 grid cell was separated as the transpiration from full vegetation cover and the evaporation from bare soil  
148 surface if energy transfer from the vegetation to the soil surface was ignored (Nishida et al., 2003), i.e.,

$$149 \quad ET = f_{veg}ET_{veg} + (1 - f_{veg})ET_{soil} \quad (1)$$

150 where the subscript "*veg*" means full vegetation cover and the subscript "*soil*" indicates the soil exposed  
151 to solar radiation (called bare soil);  $ET_{veg}$  is the transpiration from full vegetation cover area ( $\text{W m}^{-2}$ ),  
152  $ET_{soil}$  is the evaporation from bare soil ( $\text{W m}^{-2}$ ),  $f_{veg}$  is the portion of the area with the vegetation cover,  
153 which can be calculated by Normalized Difference Vegetation Index (calculation details are provided in  
154 Appendix A, Tang et al., 2009)

155 The available energy  $Q$  ( $\text{W m}^{-2}$ ), which is the sum of the latent heat flux and sensible heat flux (also  
 156 known as the net radiation minus soil heat flux) is also separated into the available energy for vegetation  
 157 transpiration,  $Q_{veg}$  ( $\text{W m}^{-2}$ ) and  $Q_{soil}$  ( $\text{W m}^{-2}$ ) for bare soil evaporation, which was expressed by Nishida  
 158 et al. (2003) as:

$$159 \quad Q = f_{veg} Q_{veg} + (1 - f_{veg}) Q_{soil} \quad (4)$$

160 As satellites like Terra and Aqua provide instantaneous snapshot observations of the Earth only once  
 161 a day, a temporal scaling method is needed to convert instantaneous measurements into daily ET values.  
 162 Nishida et al. (2003) used satellite-based noon time instantaneous evaporation fraction ( $EF$ ), defined as  
 163 the ratio of latent heat flux ( $ET$ ) to available energy as daily  $EF$  ( $EF = \frac{ET}{Q}$ , the calculation of  
 164 instantaneous  $EF$  is described at Appendix B), multiplied the daily  $Q$  to calculate daily  $ET$  based on the  
 165 assumption that  $EF$  is constant over a day:

$$166 \quad ET = EF Q \quad (5)$$

167 In the next section, we will detail how VISEA calculates the daily  $EF$ , and  $Q$  in Equation (5), and  
 168 also daily air and  $T_s$ , land surface temperature.

### 169 2.1.1 Daily evaporation fraction calculation

170 As the assumption of  $EF^i = EF^d$  caused 10%-30% underestimation of daily ET (Huang et al.,  
 171 2017; Yang et al., 2013), we introduced a decoupling parameter to convert  $EF^i$  into  $EF^d$  following the  
 172 algorithm of Tang et al. (2017a, 2017b). This new decoupling parameter-based evaporation fraction is  
 173 developed from Penman-Monteith and McNaughton-Jarvis mathematical equations:

$$174 \quad EF^d = EF^i \frac{\Delta^d}{\Delta^d + \gamma} \frac{\Delta^i + \gamma}{\Delta^i} \frac{\Omega^{*i}}{\Omega^{*d}} \frac{\Omega^d}{\Omega^i} \quad (6)$$

175 where superscript "d" means daily; the  $EF^i$  is the instantaneous evaporation fraction;  $\Omega$  is the decoupling  
 176 factor that represents the relative contribution of radiative and aerodynamic terms to the overall  
 177 evapotranspiration (Tang and Li, 2017),  $\Omega_i^*$  is the value of the decoupling factor,  $\Omega$ , for wet surfaces.  
 178 According to Pereira (2004),  $\Omega$  and  $\Omega^*$  (the calculation details is presented in Appendix C).

179 For full vegetation-covered areas,  $EF_{veg}^d$  is expressed as:

$$180 \quad EF_{veg}^d = \frac{\alpha \Delta^i}{\Delta^i + \gamma \left( 1 + \frac{r_{c\,veg}^i}{2r_{a\,veg}^i} \right)} \left( \frac{\Delta^d}{\Delta^d + \gamma} \frac{\Delta^i + \gamma}{\Delta^i} \frac{\Omega_{veg}^{*i}}{\Omega_{veg}^{*d}} \frac{\Omega_{veg}^d}{\Omega_{veg}^i} \right) \quad (7)$$

181  $r_{c\,veg}^i$  is the instantaneous canopy resistance ( $\text{s m}^{-1}$ ),  $r_{a\,veg}^i$  is the instantaneous aerodynamic resistance ( $\text{s}$   
 182  $\text{m}^{-1}$ ). Determining these resistances are presented in Appendix D.

183 For bare soil,  $EF_{soil}^d$  is calculated as:

$$184 \quad EF_{soil}^d = \frac{T_{soil\,max}^i - T_{soil}^i}{T_{soil\,max}^i - T_a^i} \frac{Q_{soil\,0}^i}{Q_{soil}^i} \left( \frac{\Delta^d}{\Delta^d + \gamma} \frac{\Delta^i + \gamma}{\Delta^i} \frac{\Omega_{soil}^{*i}}{\Omega_{soil}^{*d}} \frac{\Omega_{soil}^d}{\Omega_{soil}^i} \right) \quad (8)$$

185 Thus,  $EF^d$  is expressed as:

$$186 \quad EF^d = f_{veg} \frac{Q_{veg}^i}{Q^i} EF_{veg}^d + (1 - f_{veg}) \frac{Q_{soil}^i}{Q^i} EF_{soil}^d \quad (9)$$

### 187 2.1.2 Daily calculation of available energy $Q_{veg}^d$ and $Q_{soil}^d$

188 We used an improved daily available energy  $Q$  ( $W m^{-2}$ ) method (Huang et al., 2023) for the  
189 vegetation and the bare soil surface is calculated by the energy balance equation:

$$190 \quad R_n - G = Q \quad (10)$$

191 where  $R_n$  is the net radiation ( $W m^{-2}$ ), which could be calculated by the land surface energy balance;  $G$   
192 is the soil heat flux ( $W m^{-2}$ ),  $G \approx 0$  on a daily basis (Fritschen and Gay, 1979; Nishida et al., 2003; Tang et  
193 al., 2009),

$$194 \quad R_n^d = (1 - albedo^d)R_d^d - \varepsilon_s^d \sigma T_s^{d4} + (1 + Cloud^d)\varepsilon_a^d \sigma T_a^{d4} \quad (11)$$

195 Where  $albedo^d$  is the daily albedo of the soil surface;  $R_d^d$  is daily incoming shortwave radiation ( $W m^{-2}$ ),  
196 obtained the ERA5\_Land shortwave radiation (we called ERA5\_Rd);  $\varepsilon_s^d$  and  $\varepsilon_a^d$  are the daily  
197 emissivity of land surface and atmosphere; different from the former study provided by Huang et al.,  
198 (2021), which set we  $\varepsilon_s^d$  and  $\varepsilon_a^d$  equal, we calculated the  $\varepsilon_a^d$  by Appendix E flowing study of Brutsaert,  
199 (1975) and Wang and Dickinson(2013),  $\varepsilon_s^d$  can be retried by MOD11C1;  $\sigma$  is the Stefan-Boltzmann  
200 constant;  $T_a^d$  is the daily near surface air temperature (K);  $T_s^d$  is the daily surface temperature (K).

201 We account for the influence of clouds by assuming a linear correlation between downward  
202 longwave radiation and cloud coverage in the calculation of downwards longwave radiation based on the  
203 study of Huang et al., (2023):

$$204 \quad Cloud = (1 - K_t) \quad (12)$$

$$205 \quad K_t = \frac{R_d^d}{R_a^d} \quad (13)$$

206  $Cloud^d$  is derived from the clearness index  $K_t$  (Chang and Zhang, 2019; Goforth et al., 2002).  $R_a^d$  is the  
207 daily extraterrestrial radiation calculated by the FAO (1998).

208 According to Huang et al. (2023),  $Q_{veg}^d$  can be calculated by assuming as  $T_s^d = T_a^d$  according to the  
209 VI-Ts method which implies that the minimum land surface temperature occurs in fully vegetated grid  
210 cells and is equivalent to  $T_a^d$ .

$$211 \quad Q_{veg}^d = (1 - albedo^d)R_d^d + (1 + Cloud^d)\varepsilon_a^d \sigma T_a^{d4} - \varepsilon_s^d \sigma T_s^{d4} \quad (14)$$

$$212 \quad Q_{soil}^d = (1 - C_G)(1 - albedo^d)R_d^d + (1 + Cloud^d)\varepsilon_a^d \sigma T_a^{d4} - \varepsilon_s^d \sigma T_s^{d4} \quad (15)$$

213 Thus,  $(1 + Cloud^d)\varepsilon_a^d \sigma T_a^{d4}$  is the daily downward longwave radiation ( $W m^{-2}$ ), and  $\varepsilon_s^d \sigma T_s^{d4}$  is the

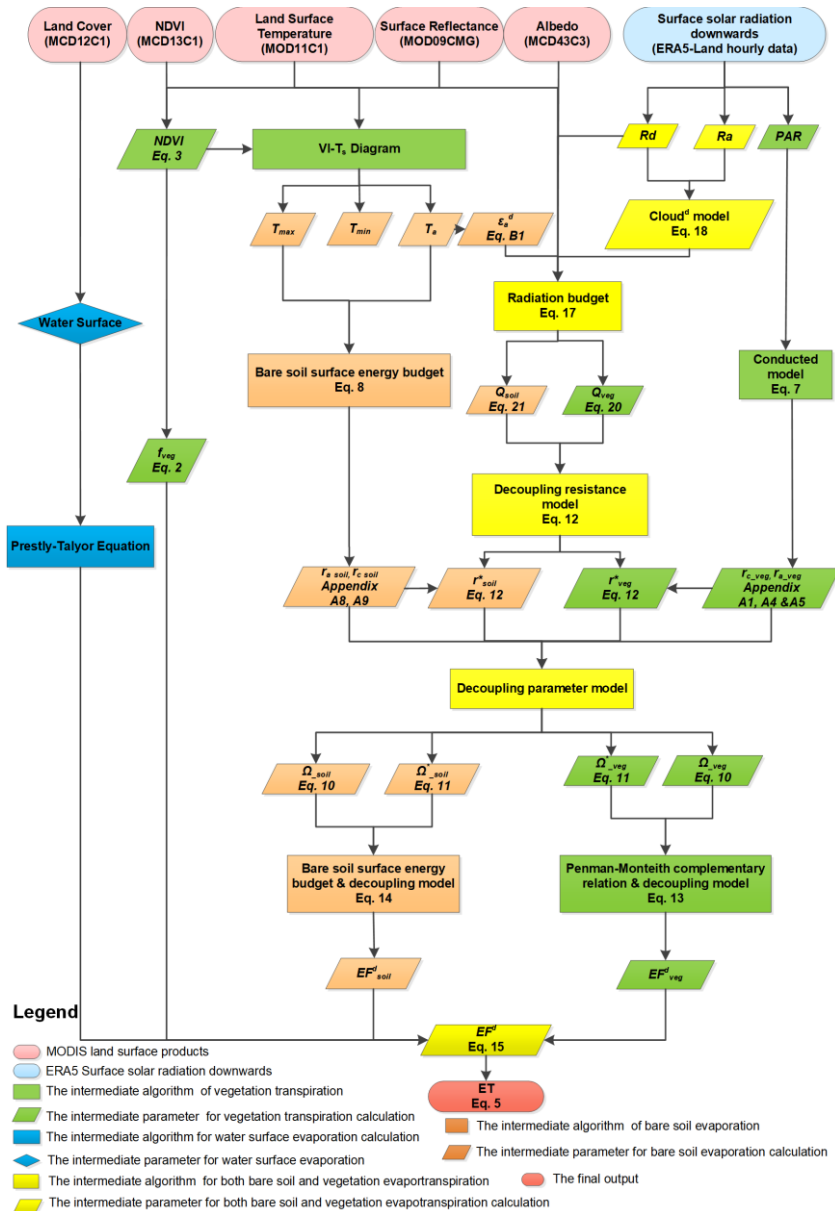
214 daily upward longwave radiation ( $W m^{-2}$ ), where  $C_G$  is an empirical coefficient ranging from 0.3 for a  
 215 wet soil to 0.5 for a dry soil (Idso et al., 1975).

216 Following the study of Huang et al. (2023), the daily  $ET^d$  can be calculated by the daily  $EF^d$  and  
 217  $Q^d$  as:

$$218 \quad ET^d = EF^d Q^d \quad (16)$$

219 Figure 1 illustrates the workflow of VISEA.

220



221

222 **Figure 1.** Schematic of VISEA algorithm. The ovals in the top row are the databases, and the square  
 223 boxes are the algorithms, and parallelograms are the parameters. The numbers in the parenthesis are the  
 224 equation to determine the parameters.

225

226 **2.1.3 The calculation of daily air temperature,  $T_a^d$  and surface temperature,  $T_s^d$**

227 Daily air temperature,  $T_a^d$  is a critical parameter in the VISEA algorithm, used in calculations for  
228 downward longwave radiation, daily aerodynamic resistance, and surface resistance. The key innovation  
229 in calculating  $T_a^d$ , involves employing the VI-Ts method to estimate instantaneous air temperature,  $T_a^i$   
230 during the daytime.

231 This method was developed based on the empirical linear relationship between surface temperature  
232 (Ts) and Vegetation Index (VI). Surface temperature increases when the vegetation index decreases, and  
233 conversely, surface temperature decreases when the vegetation index increases. By defining a "window"  
234 formed by the neighboring 5 \* 5 grid cells, the scatter plot of these 25 grid cells' VI and Ts typically  
235 exhibits a triangular (or trapezoidal) distribution. In this scatter plot, we identify the "warm edge"  
236 (characterized by a low vegetation cover fraction and high Ts) and the "cold edge" (marked by a high  
237 vegetation cover fraction and low Ts).

238 Through simple interpolation, Ts corresponding to any given vegetation condition within the range  
239 of the "warm edge" and "cold edge" can be determined. The lowest Ts could be determined by the highest  
240 VI, and the highest Ts could be determined by the lowest VI. Therefore, following Nishida et al. (2003),  
241 under the assumption that the lowest surface temperature equals the air temperature (Ta), we can derive  
242 the daily air temperature.

243 For nighttime periods, it is assumed that air temperature is equivalent to the nighttime land surface  
244 temperature provided by MOD11C1. These two temperature estimates are then extended into hourly air  
245 temperature profiles using a sine-cosine fitting curve. The 24-hour average of  $T_a^i$  is used as  $T_a^d$ . Similarly,  
246  $T_s^d$  is calculated using MOD11C1 land surface temperature data for both daytime and nighttime. These  
247 estimates are extended into hourly surface temperature profiles using a similar sine-cosine fitting curve,  
248 and the daily average of  $T_s^d$  is determined (Huang et al., 2021).

249 A key advance of this VISEA algorithm is the application of the VI-Ts method to calculate  $T_{soil\ max}^i$   
250 and  $T_a^i$  (Huang et al., 2017; Nishida et al., 2003; Tang et al., 2009). The VI-Ts method is based on the  
251 empirical linear relationship between the vegetation index (VI), typically calculated by NDVI, and land  
252 surface temperature (Ts). When plotted on a two-dimensional scatter plot, VI and Ts generally form a  
253 trapezoid or triangular shape. In these plots, regions with low VI and high Ts values constitute the "warm  
254 edge," while areas with high VI and low Ts values form the "cold edge." Using simple linear interpolation,  
255 Ts values corresponding to any given VI between the "warm edge" and the "cold edge" can be determined.  
256 Assuming  $T_s = T_a^i$  for cases where the highest VI corresponds to the lowest Ts, we can calculate  $T_a^i$ .  
257 Similarly,  $T_{soil\ max}^i$  can be easily calculated since it corresponds to the lowest VI.

258 This VI-Ts method allows for the estimation of  $T_a^i$  and  $T_{soil\ max}^i$  without the need for additional  
259 meteorological data. However, some studies have found that the VI-Ts method may not consistently



260 provide satisfactory results, especially in colder regions where vegetation thrives better under higher  
261 temperatures.

## 262 **2.2 Technical validation**

263 The correlation coefficient, Root Mean Square Error (RMSE) and Nash-Sutcliffe efficiency coefficient  
264 are used to evaluate our global daily ET estimates with eddy covariance measurements and compared  
265 with the other five independent global ET products on a monthly scale.

266 The correlation coefficient  $R$  is calculated as:

$$267 \quad R = \frac{\sum(X-\bar{X})(Y-\bar{Y})}{\sqrt{\sum(X-\bar{X})^2 \sum(Y-\bar{Y})^2}} \quad (17)$$

268  $R$  is the correlation coefficient;  $X$  is the estimated variable;  $\bar{X}$  is the average of  $X$ ;  $Y$  is the observed  
269 variable;  $\bar{Y}$  is the average of  $Y$ .

270 The Root Mean Square Error (RMSE) is calculated as:

$$271 \quad RMSE = \sqrt{\frac{\sum_{i=1}^N (X_i - Y_i)^2}{N}} \quad (18)$$

272 For a more nuanced understanding of the Root Mean Square Error (RMSE), we have deconstructed  
273 it into two distinct components: RMSEs (systematic RMSE) and RMSEu (unsystematic RMSE). This  
274 breakdown allows a more detailed examination of the systematic and unsystematic sources contributing  
275 to the overall error metric.

276 The systematic Root Mean Square Error (RMSEs) is calculated as:

$$277 \quad RMSEs = \sqrt{\frac{\sum_{i=1}^N (Z_i - Y_i)^2}{N}} \quad (19)$$

278 The unsystematic Root Mean Square Error (RMSEu) is calculated as:

$$279 \quad RMSEu = \sqrt{\frac{\sum_{i=1}^N (Z_i - X_i)^2}{N}} \quad (20)$$

280 Where  $Z_i = a + bY_i$ , where  $a$  and  $b$  are the least squares regression coefficients of the estimated variable  
281  $X_i$  and observed variable  $Y_i$ ,  $N$  is the sample size (Norman et al., 1995).

282 The Nash-Sutcliffe efficiency coefficient (NSE)

$$283 \quad NSE = 1 - \frac{\sum(X_i - Y_i)^2}{\sum(Y_i - \bar{Y})^2} \quad (21)$$

284 The ratio of the standard deviations of  $X$  and  $Y$

285 
$$Ratio = \frac{X_{Standard\ Deviation}}{Y_{Standard\ Deviation}} \quad (22)$$

286 The Bias of  $X$  and  $Y$

287 
$$Bias = \bar{X} - \bar{Y} \quad (23)$$

288 **2.3 The gap-filling of MODIS data**

289 MODIS sensors on board of Terra and Aqua observe the Earth twice a day. However, there are  
 290 always data gaps in the MODIS land products because of cloud cover problems. In the VISEA algorithm,  
 291 we used the neighboring days' available data to fill the data gaps. According to the study of Tang et al.  
 292 (2009), the cloud gaps don't reduce the accuracy of this algorithm significantly.

293 **3. Data**

294 **3.1 The input data**

295 The input data including the MODIS land products: daily 0.05° surface reflectance (MOD09CMG),  
 296 land surface temperature/emissivity (MOD11C1) and albedo (MCD43C3), 8-day 0.05° vegetation  
 297 indices (MOD13C1) and yearly 0.05° land cover products (MCD12C1). We also used hourly downward  
 298 surface solar radiation from the Fifth Generation of the European Centre for Medium-Range Weather  
 299 Forecasts (ECMWF) Reanalysis (ERA5), "ERA5-Land hourly data from 1950 to present" data as energy  
 300 input of VISEA algorithm. The surface solar radiation data from ERA5-Land and land data products from  
 301 MODIS land products are both near-real-time datasets with a one-week delay, enabling VISEA to provide  
 302 global near-real-time ET estimations. Details of the input data, their download links, variable names, used  
 303 parameters, spatial and temporal resolution are given in Table 1.

304 **Table 1. The input of VISEA**

<b>The input of VISEA</b>			
<b>Data source</b>	Data name	Used parameter	Spatial/temporal resolution
<b>MODIS Land Product</b>	MOD11C1	Land Surface Temperature	0.05°/ daily
	MOD09CMG	Surface Reflectance	0.05°/daily
	MCD43C3	Albedo	0.05°/daily
	MOD13C1	NDVI	0.05°/16-day
	MCD12C1	Land cover	0.05°/ yearly
<b>ERA5-Land hourly data</b>	Rd	Downward surface solar radiation	0.1°/ hourly

305

306 **3.2 The evaluation data**

### 307 **3.2.1 The flux tower measurements from FLUXNET**

308 We evaluated the accuracy of the input ERA5-Land shortwave radiation, estimated daily net radiation,  
309 air temperature, and ET by comparing them against measurements from FLUXNET2015 (Pastorello et  
310 al., 2020). The data from FLUXNET2015 can be obtained at <https://fluxnet.org/data/download-data>.  
311 While there are records from a total of 212 flux towers in our datasets, not all of them met our stringent  
312 inclusion criteria. Each site needed to fulfil three specific requirements to be included in our analysis: (1)  
313 availability of data for the period spanning from 2001 to 2015; (2) ERA5-Land downward shortwave  
314 radiation greater than 0 within the  $0.1^\circ \times 0.1^\circ$  grid cell corresponding to the flux tower's location; (3)  
315 conformity with MODIS land cover data (MOD12C1) at the  $0.05^\circ \times 0.05^\circ$  grid cell level, ensuring that  
316 the flux tower was situated on land rather than over the ocean. In our evaluation using FLUXNET  
317 observational data, we leveraged FLUXNET's diligent efforts in addressing energy closure concerns.  
318 Specifically, FLUXNET has implemented rigorous measures for energy closure corrections and  
319 validations, thereby enhancing the reliability of the observational data from the 212 globally distributed  
320 flux towers (Pastorello et al., 2020; Baldocchi et al., 2001; Wang et al., 2022), We selected data spanning  
321 the period from 2001 to 2015 and excluded sites where ERA5-Land downward shortwave radiation was  
322 zero.

323 Our study incorporates data from a carefully selected subset of 149 flux towers that met these  
324 stringent criteria. This approach ensures the reliability and relevance of our analysis. The distribution of  
325 these 149 flux towers is presented in Figure 2. Supplementary Table S1 shows the longitude, latitude,  
326 elevation, and land cover type (classified by the International Geosphere-Biosphere Programme, IGBP)  
327 of these sites. The 149 sites covered 12 IGBP land cover types: 18 croplands (CRO), 1 closed shrublands  
328 (CSH), 15 deciduous broadleaf forests (DBF), 1 deciduous needle leaf forest (DNF), 10 evergreen  
329 broadleaf forests (EBF), 34 evergreen needle leaf forests (ENF), 30 grasslands (GRA), 5 mixed forests  
330 (MF), 8 open shrublands (OSH), 8 savannas (SAV), 13 wetlands (WET), and 6 woody savannas (WSA).

### 331 **3.2.2 The other gridded ET and precipitation products**

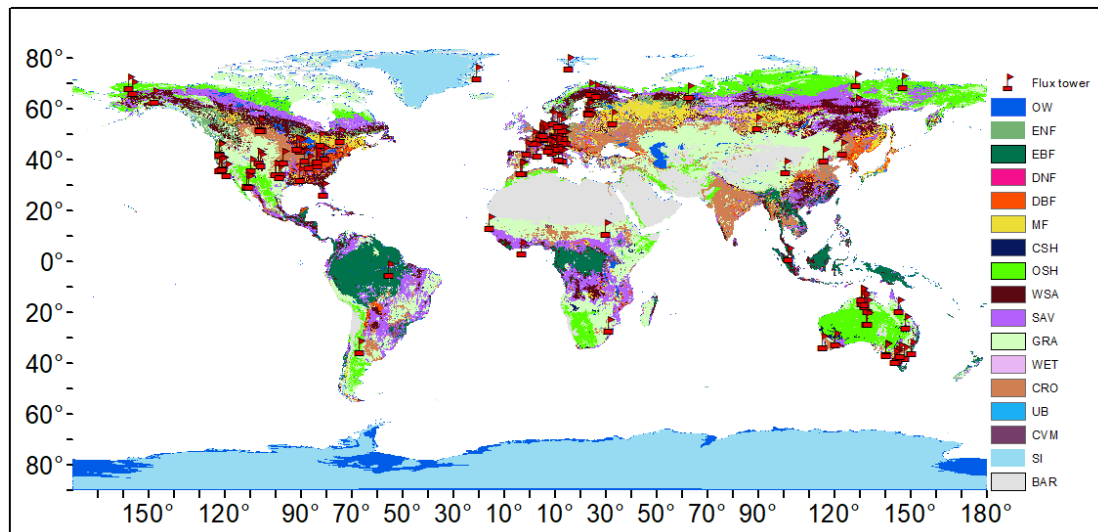
332 We also used five independent globally gridded ET and one precipitation products for VISEA estimated  
333 ET's comparison. The five ET products include two MODIS-based ET products: MOD16 (Mu et al.,  
334 2007, 2011) and Penman-Monteith-Leuning Evapotranspiration V2 (PML) (Zhang et al., 2019, 2022),  
335 one AVHRR-based AVHRR ET (Zhang et al., 2009, 2010), one machine learning algorithm output, the  
336 FLUXCOM ET data (Jung et al., 2009, 2010, 2018, 2019) and one multiple-satellites data based Global  
337 Land Evaporation Amsterdam Model (GLEAM) ET (Martens et al., 2017; Miralles et al., 2011). The  
338 precipitation data was from the Global Precipitation Climatology Centre (GPCC), which is based on local  
339 measurements (Schneider et al., 2014, 2017; Becker et al., 2013) and Global Unified Gauge-Based  
340 Analysis of Daily Precipitation (GPC). Details of these five ET products and the precipitation data are  
341 given in Table 2. To maintain the consistency in temporal and spatial resolution for comparison purposes,  
342 we obtained monthly MOD16 and PML, despite their original temporal resolution of 8 days and used the  
343  $0.05^\circ \times 0.05^\circ$  version of MOD16, AVHRR ET and PML. Additionally, for multi-year scale comparisons,  
344 we confined our dataset to the timeframe between 2001 and 2020. We also incorporated daily  
345 Evapotranspiration (ET) data from GLEAM and VISEA, alongside precipitation data from the Climate

346 Prediction Center (CPC), spanning from July 25<sup>th</sup> to August 2<sup>nd</sup>, 2022. This allowed for near-real-time  
 347 analysis of ET and precipitation during the Yangtze River drought incident within that interval, despite  
 348 the datasets potentially encompassing more extensive periods.

349 **Table 2.** The five global girded ET products and one precipitation product used for comparison with our  
 350 near-real-time global daily terrestrial ET estimates.

Product name	Spatial/Temporal resolution	Time period	Theory
GLEAM	0.25°/Monthly	2001-2022	Priestly-Taylor Equation
FLUXCOM	0.5°/Monthly	2001-2016	Machine learning
MOD16	0.05°/Monthly	2001-2014	Penman-Monteith Equation
AVHRR	1°/Monthly	2001-2006	Improved Penman-Monteith Equation
PML	0.05°/8-day	2003-2018	Penman-Monteith Equation and a diagnostic biophysical model
GPCC	0.25°/Monthly	2001-2019	in-situ observations
GPC	0.5°/Daily	08/28/2022-09/01/2022	Global Unified Gauge-Based Analysis of Daily Precipitation

351



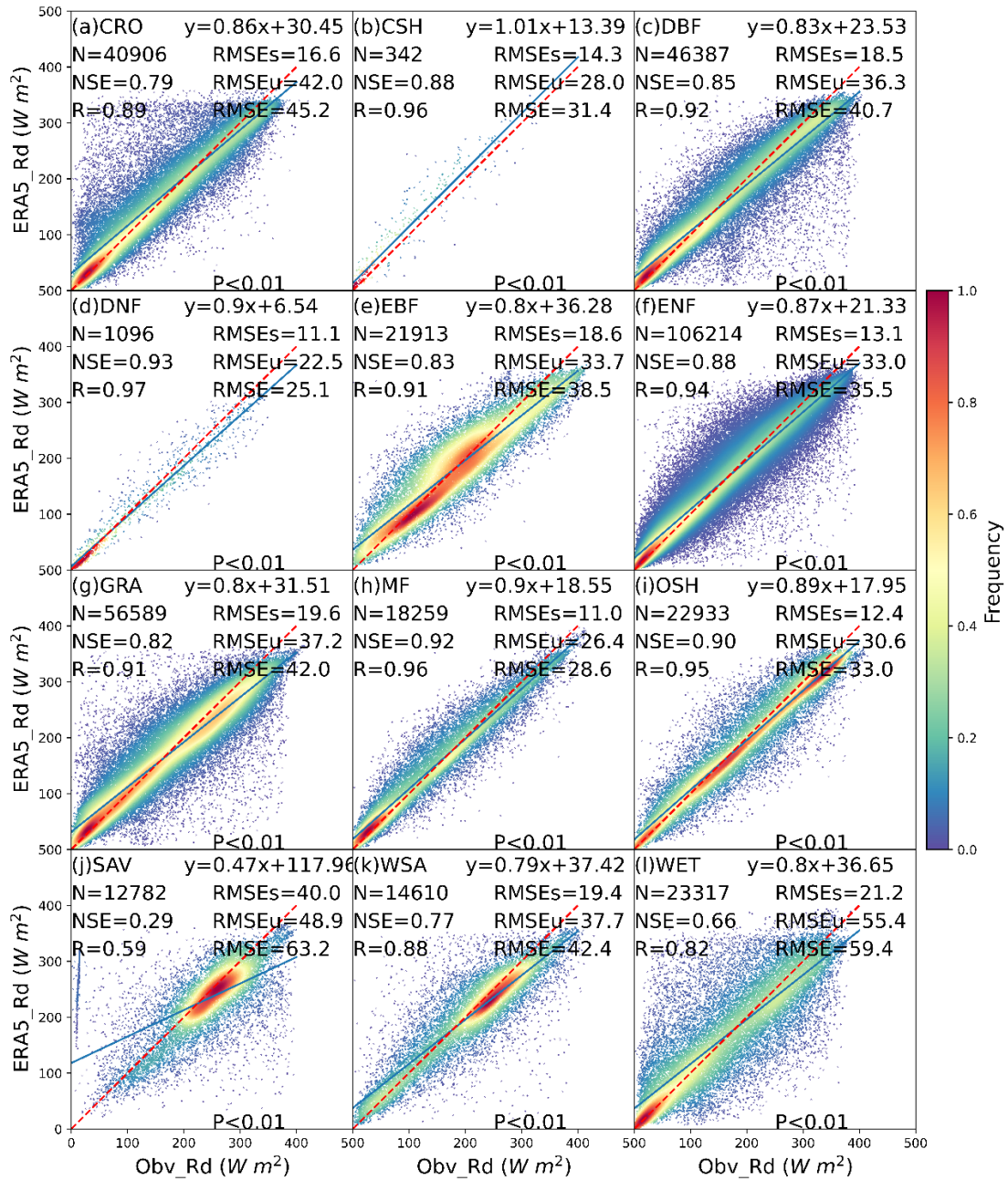
352

353

354 **Figure 2.** The distribution of 149 flux towers from FLUXNET in different IGBP land cover types,  
 355 specifically OW (Water bodies), ENF (Evergreen needle leaf forests), EBF (Evergreen broadleaf forests),  
 356 DNF (Deciduous needle leaf forests), DBF (Deciduous broadleaf forests), MF (Mixed forests), CSH  
 357 (Closed shrublands), OSH (Open shrublands), WSA (Woody savannas), SAV (Savannas), GRA  
 358 (Grasslands), WET (Permanent wetlands), CRO (Croplands), UB (Urban and built-up lands), CVM  
 359 (Cropland/natural vegetation mosaics), SI (Snow and ice), BAR (Barren).

360 **4. Results**

361 In our initial analysis, we juxtaposed downward solar radiation input data from ERA5-Land  
 362 (ERA5\_Rd) with measurements obtained from 149 flux towers (Obv\_Rd) across diverse IGBP land cover  
 363 types, as illustrated in Figure 3. The results indicate a commendable agreement between ERA5\_Rd and  
 364 Obv\_Rd measurements for the majority of land covers, with notable exceptions observed in savanna  
 365 (SAV). Specifically, the mean Nash-Sutcliffe Efficiency (NSE) stands at 0.84, the mean correlation  
 366 coefficient (R) at 0.92, and the mean Root Mean Square Error (RMSE) at 38.3 W m<sup>-2</sup>. This comparative  
 367 analysis offers helpful insights into the performance of ERA5\_Rd across different land cover categories.



368

369 **Figure 3.** The scatter plot of downward solar radiation from ERA5-Land (ERA5\_Rd) compared with  
370 local instruments measurements (Obv\_Rd) under 12 IGBP land cover types: CRO (Croplands), CSH  
371 (Closed shrublands), DBF (Deciduous broadleaf forests), DNF (Deciduous needle leaf forests), EBF  
372 (Evergreen broadleaf forests), ENF (Evergreen needle leaf forests), GRA (Grasslands), MF (Mixed  
373 forests), OSH (Open shrublands), SAV (Savannas), WSA (Woody savannas), WET (Permanent  
374 wetlands). The red dotted line is the 1:1 line. N is the number of data points, NSE is Nash-Sutcliffe  
375 Efficiency, R is correlation coefficients, RMSE is Root Mean Square Error, RMSEs is systematic RMSE,  
376 and RMSEu is unsystematic RMSE. The Frequency denotes the probability density estimated through  
377 the KDE method with a Gaussian kernel, and it is then scaled to ensure that the maximum value of the  
378 probability density function equals 1. P is the P-Value for the Correlation Coefficient.

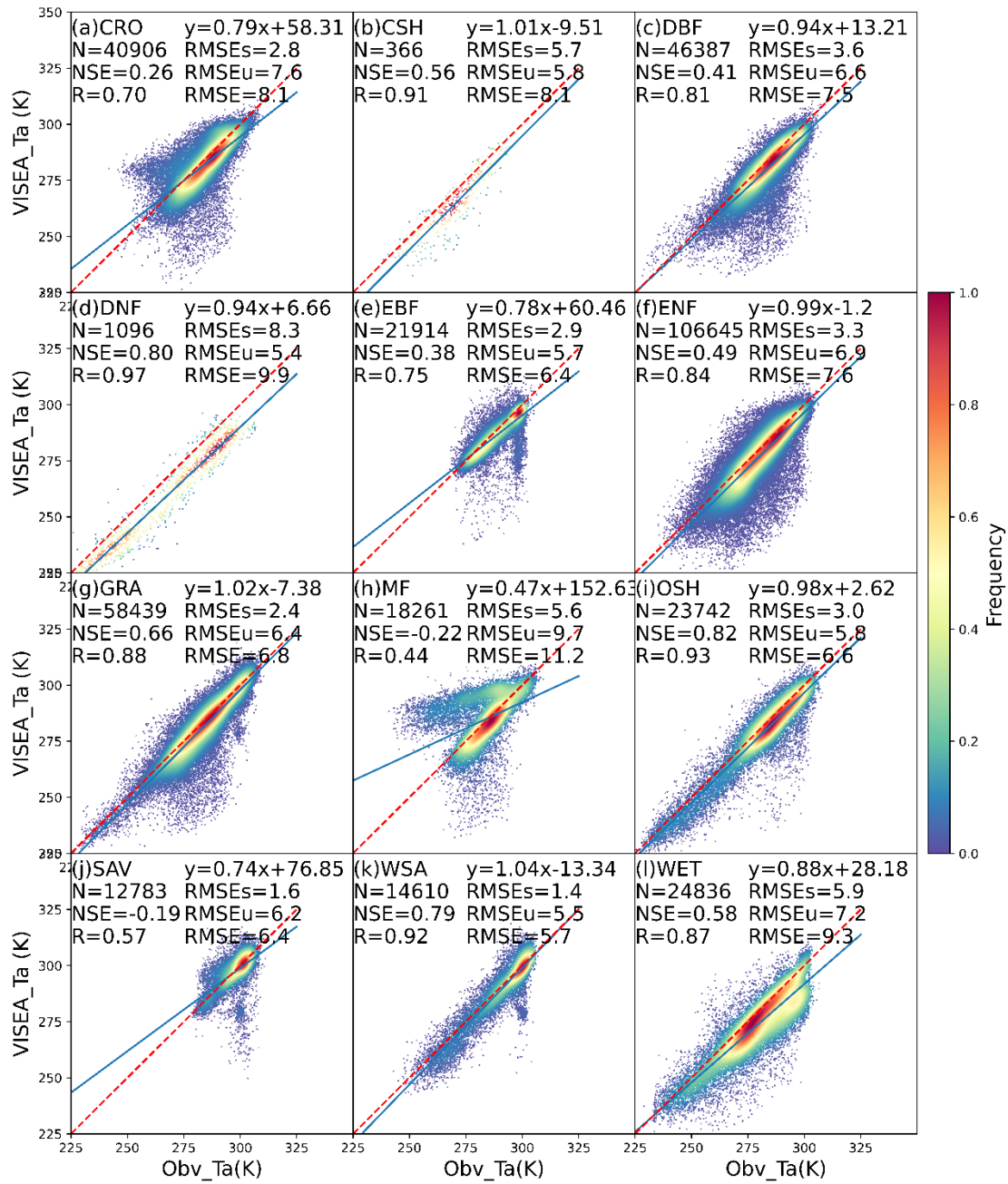
379 In Figure 3, ERA5\_Rd exhibits optimal performance in DNF and MF, reflected by NSE and R values  
380 surpassing 0.9. In these land covers, the mean RMSEs stand at  $11 \text{ W m}^{-2}$ , mean RMSEu at  $24.5 \text{ W m}^{-2}$ ,  
381 and mean RMSE at  $26.9 \text{ W m}^{-2}$ . However, its performance in SAV is notably subpar, characterized by  
382 an NSE of 0.29, an R of 0.59, highest RMSEs of  $40 \text{ W m}^{-2}$ , RMSEu of  $48.9 \text{ W m}^{-2}$ , and RMSE of  $63.2$   
383  $\text{W m}^{-2}$ . For ERA5\_Rd, the mean RMSEs amount to  $16 \text{ W m}^{-2}$ , and the mean RMSEu is  $34.8 \text{ W m}^{-2}$ ,  
384 suggesting that ERA5\_Rd demonstrates high accuracy by effectively capturing the systematic variation  
385 in Obv\_Rd, as indicated by its relatively low RMSEs and RMSEu close to RMSE (Willmott et al., 1981)  
386 in most land covers, except for SAV. Specifically, we have annotated the figure to indicate that all Rd  
387 values derived from ERA5 exhibit very low P-values ( $<0.01$ ). This indicates a statistically significant  
388 correlation between the input shortwave radiation from ERA5 and the local measurements.

389 Several factors come into play in understanding the disparities in performance in downward solar  
390 radiation of ERA5 (ERA5\_Rd) across different land cover types. In regions characterized by denser  
391 forests, such as DNF and MF, ERA5\_Rd's superior performance may be attributed to the lower density  
392 of ground-based meteorology stations (DNF,  $N = 1096$ ) and the relatively uniform subsurface and canopy  
393 coverage in MF, facilitating a more accurate representation in the ERA5 radiative transfer model.  
394 Conversely, savannas present unique challenges due to sparse vegetation and flat terrain, influencing  
395 sunlight transmission dynamics (Yang and Friedl, 2003). Land-use changes, including farming and urban  
396 development, further complicate the accuracy of sunlight transmission (Wang et al., 2014; Zhang et al.,  
397 2022). Additionally, factors like aerosols from natural or anthropogenic sources contribute to data  
398 variations (Naud et al., 2014; Wang et al., 2021b). The inaccuracies in accounting for the rainy season,  
399 leading to increased cloud cover and rainfall in savannas, contribute to ERA5\_Rd's limitations (Jiang et  
400 al., 2020).

401 Our local scale evaluation, as demonstrated in Figure 3, supports our stance that this resolution  
402 disparity between MODIS Land product at  $0.05^\circ$  and ERA5 data at  $0.1^\circ$  minimally impacts the final ET  
403 product's accuracy. This approach is consistent with the methodologies adopted in the studies by Huang  
404 et al. (2017, 2021, 2023), which effectively utilized MODIS land products at a  $0.05^\circ$  resolution in  
405 conjunction with downward shortwave radiation data at a  $0.1^\circ$  resolution from the China Meteorology  
406 Forcing Dataset. Such precedents underscore the feasibility of integrating these resolutions for ET

407 estimation, bolstering our confidence in the methodological integrity of our study despite the noted  
 408 resolution differences.

409 Figure 4 depicts scatter plots illustrating the comparison between the estimated air temperature using  
 410 the VI-T<sub>s</sub> method (VISEA\_Ta) and local meteorological measurements (Obv\_Ta). The analysis reveals  
 411 that VISEA\_Ta generally aligns with Obv\_Ta, exhibiting NSE values ranging from -0.22 (MF) to 0.82  
 412 (OSH), R values ranging from 0.44 (MF) to 0.97 (DNF), and RMSE values ranging from 5.7 K (WSA)  
 413 to 11.2 K (MF). Particularly noteworthy is VISEA\_Ta's outstanding performance at OSH (NSE = 0.82,  
 414 R = 0.93, RMSE = 6.6 K), WSA (NSE = 0.79, R = 0.92, RMSE = 5.7 K) and GRA (NSE = 0.66, R =  
 415 0.88, RMSE = 6.8 K).



416

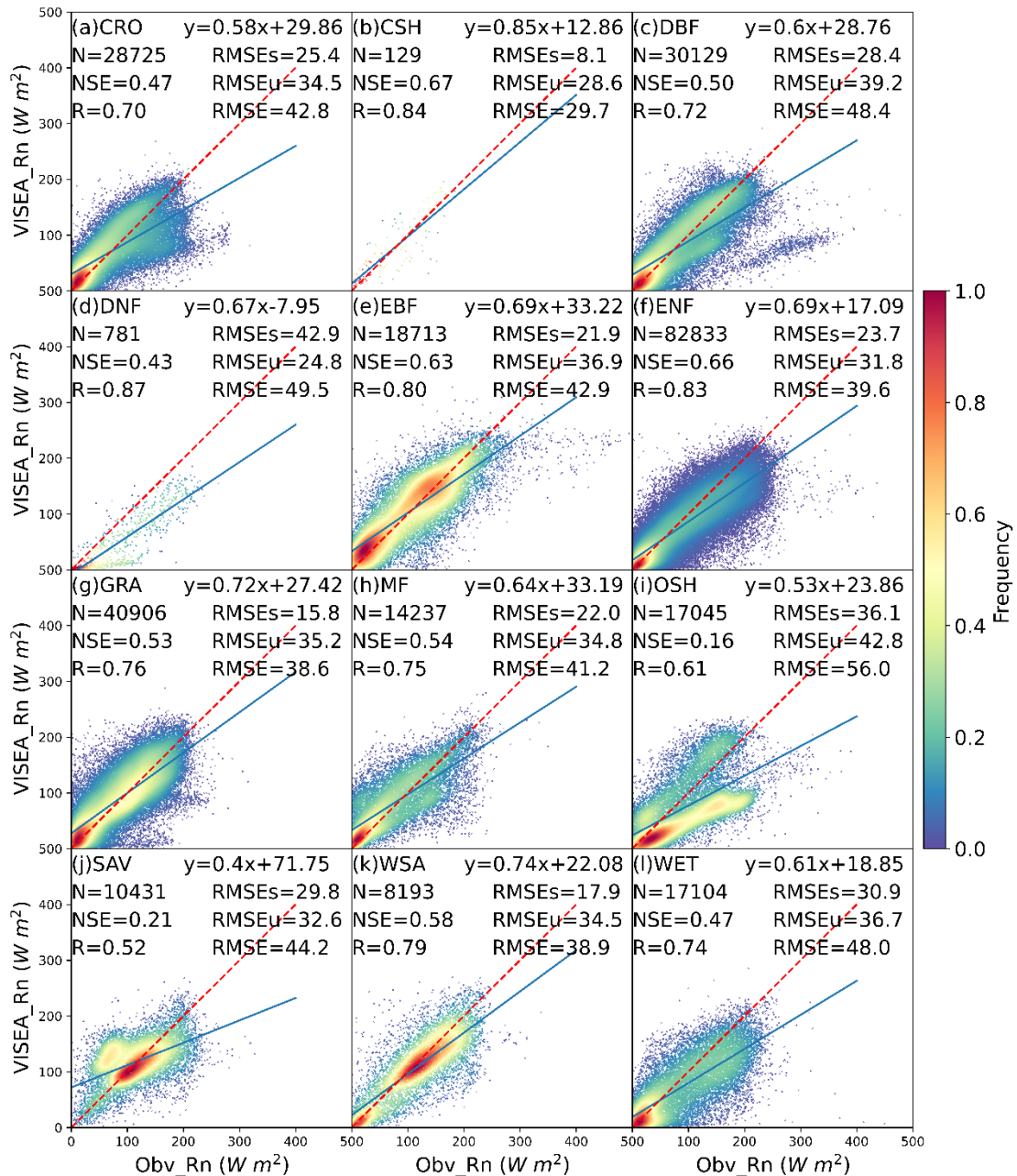
417 **Figure 4.** The scatter plot of daily air temperature simulated by VISEA (VISEA\_Ta) compared with local  
418 instruments measurements (Obv\_Ta) under 12 IGBP land cover types: CRO (Croplands), CSH (Closed  
419 shrublands), DBF (Deciduous broadleaf forests), DNF (Deciduous needle leaf forests), EBF (Evergreen  
420 broadleaf forests), ENF (Evergreen needle leaf forests), GRA (Grasslands), MF (Mixed forests), OSH  
421 (Open shrublands), SAV (Savannas), WSA (Woody savannas), WET (Permanent wetlands). The red  
422 dotted line is the 1:1 line. N is the number of data points, NSE is Nash-Sutcliffe Efficiency, R is  
423 correlation coefficients, RMSE is Root Mean Square Error, RMSEs is systematic RMSE, and RMSEu is  
424 unsystematic RMSE. The frequency denotes the probability density estimated through the Kernel Density  
425 Estimation, KDE method with a Gaussian kernel, and it is then scaled to ensure that the maximum value  
426 of the probability density function equals 1.

427 Conversely, its least satisfactory performance is evident at MF (NSE = -0.22, R = 0.44, RMSE =  
428 11.2 K), SAV (NSE = -0.19, R = 0.57, RMSE = 6.4 K), and CRO (NSE = 0.26, R = 0.70, RMSE = 8.1  
429 K). The RMSEs are lower than RMSEu in most land cover sites, except in DNF. Despite VISEA\_Ta  
430 displaying a high NSE of 0.8 and R of 0.97 at DNF, it exhibits higher RMSEs (8.3 K) compared to  
431 RMSEu (5.4 K), indicating a systematic underestimation of VISEA\_Ta at DNF.

432 As detailed in Section 2.4, the VI-Ts method relies on a negative correlation between vegetation  
433 coverage (VI) and land surface temperature (Ts), ideally suited for cases with significant VI and Ts  
434 differences. However, for land cover types like DNF and MF situated in temperate regions with distinct  
435 seasons and cool to cold climates, the assumed negative correlation breaks down. In these regions, the  
436 positive correlation between VI and Ts, driven by vegetation growth proportional to rising Ts, results in  
437 the failure of the VI-Ts method. The challenges persist in SAV, where the VI-Ts method encounters  
438 difficulties during both dry and wet seasons. In the dry season, the method falters due to the prevalence  
439 of bare soil, resulting in VI values approaching zero and homogeneous high Ts values. Conversely, the  
440 wet season presents challenges with both VI and Ts exhibiting relatively high values and limited  
441 variances between grid cells, ultimately undermining the accuracy of VISEA\_Ta estimation.

442 The simulated daily net radiation (VISEA\_Rn) from VISEA is assessed against local meteorological  
443 measurements (Obv\_Rn) in Figure 5. In contrast to the satisfactory performance of ERA5\_Rd in Figure  
444 3, VISEA\_Rn exhibits more notable discrepancies, characterized by significant underestimation  
445 compared to Obv\_Rn. This is reflected in the mean NSE of 0.49, mean R of 0.74, and mean RMSE of  
446 43.3 W m<sup>-2</sup>. Specifically, VISEA\_Rn demonstrates good accuracy in certain land cover types, including  
447 CHS with an NSE of 0.67, R of 0.84, and RMSE of 29.7 W m<sup>-2</sup>, EBF with an NSE of 0.63, R of 0.8, and  
448 RMSE of 42.9 W m<sup>-2</sup>, and ENF with an NSE of 0.66, R of 0.83, and RMSE of 39.6 W m<sup>-2</sup>. However, its  
449 performance diminishes notably at OSH, where it records an NSE of 0.16, R of 0.61, and RMSE of 56  
450 W m<sup>-2</sup>, as well as in SAV, with an NSE of 0.21, R of 0.52, and RMSE of 44.2 W m<sup>-2</sup>. While VISEA\_Rn  
451 appears to have lower accuracy compared to ERA5\_Rd, in the majority of land cover types, the RMSEs  
452 are smaller than RMSEu, with mean RMSEs of 25.2 W m<sup>-2</sup> and mean RMSEu of 34.3 W m<sup>-2</sup>. Moreover,  
453 the RMSEu of 43.3 W m<sup>-2</sup> is almost the same as the RMSE. These findings suggest that VISEA\_Rn  
454 demonstrates fewer systematic biases, with unsystematic RMSEu contributing the most to the overall  
455 RMSE.





456

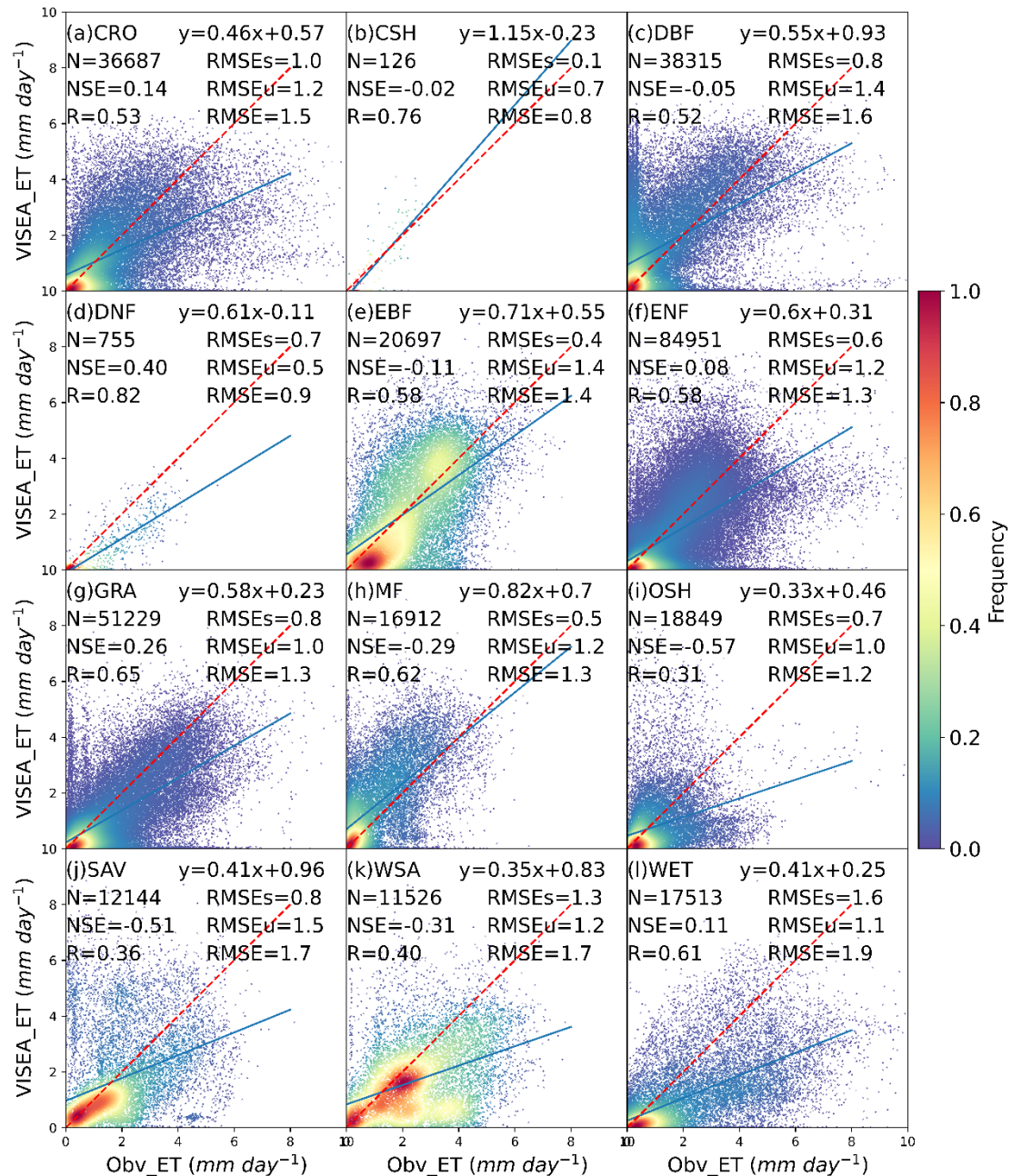
457 **Figure 5.** The scatter plot of daily net radiation simulated by VISEA (VISEA\_Rn) compared with local  
 458 instruments measurements (Obv\_Rn) under 12 IGBP land cover types: CRO (Croplands), CSH (Closed  
 459 shrublands), DBF (Deciduous broadleaf forests), DNF (Deciduous needle leaf forests), EBF (Evergreen  
 460 broadleaf forests), ENF (Evergreen needle leaf forests), GRA (Grasslands), MF (Mixed forests), OSH  
 461 (Open shrublands), SAV (Savannas), WSA (Woody savannas), WET (Permanent wetlands). The red  
 462 dotted line is the 1:1 line. N is the number of data points, NSE is Nash-Sutcliffe Efficiency, R is  
 463 correlation coefficients, RMSE is Root Mean Square Error, RMSEs is systematic RMSE, and RMSEu is  
 464 unsystematic RMSE. The frequency denotes the probability density estimated through the Kernel Density  
 465 Estimation, KDE method with a Gaussian kernel, and it is then scaled to ensure that the maximum value  
 466 of the probability density function equals 1.

467 In the context of VISEA\_Rn, a consistent pattern of approximately 30% underestimation in net  
468 radiation across various land cover types raises noteworthy discussions. This systematic discrepancy  
469 could be linked to the disparity in vegetation coverage between the observed sites' footprint and the mean  
470 vegetation coverage of the  $0.05^\circ \times 0.05^\circ$  grid cell. Specifically, the lower albedo within the footprint,  
471 compared to the grid cell's average albedo (as expressed by Eq. 14, contributes to the underestimation of  
472 Obv\_Rn. This is particularly evident in OSH, where the vegetation coverage within the footprint  
473 significantly exceeds the mean vegetation coverage of the grid cell (<0.2 compared to >0.5). Additionally,  
474 factors such as the bias in ERA5\_Rd (refer to Fig. 3, j) and VISEA\_Ta (refer to Fig. 4, j) contribute to  
475 the underestimation of VISEA\_Rn in SAV. Moreover, a substantial 50% underestimation in DNF results  
476 from the underestimated VISEA\_Ta (refer to Fig. 4, d), leading to a subsequent underestimation of  
477 downward long-wave radiation. Unpacking these intricacies sheds light on the nuanced interplay of  
478 variables influencing the observed underestimation trends in VISEA\_Rn across diverse land cover types.

479 Figure 6 illustrates scatter plots of daily evapotranspiration (ET) simulated by VISEA (VISEA\_ET)  
480 against eddy covariance measurements obtained from 149 flux tower sites (Obv\_ET) across 12 IGBP  
481 land cover types. The scatter plots of VISEA\_ET reveal a dispersed distribution, as evidenced by an  
482 average NSE of -0.08, average R of 0.56, and average RMSE of  $1.4 \text{ mm day}^{-1}$ . Notably, VISEA\_ET tends  
483 to underestimate daily ET across most land cover types. Among the 12 land cover types, VISEA\_ET  
484 exhibits the highest accuracy in DNF, with an NSE of 0.4, an R of 0.82, and an RMSE of  $0.9 \text{ mm day}^{-1}$ .  
485 It was closely followed by GRA, with NSE values of 0.26, R values of 0.65, and RMSE values of  $1.3$   
486  $\text{mm day}^{-1}$ . However, for CRO, ENF, and WET land cover types, the NSE values, although above 0, are  
487 close to 0 (mean NSE of 0.11), with a mean R of 0.53 and a mean RMSE of  $1.3 \text{ mm day}^{-1}$ . In the remaining  
488 land cover types, particularly in OSH and SAV, VISEA\_ET appears to struggle in aligning with local  
489 measurements, resulting in NSE values of -0.57 and -0.51, R values of 0.31 and 0.36, and RMSE values  
490 of  $1.2 \text{ mm day}^{-1}$  and  $1.7 \text{ mm day}^{-1}$ , respectively. As the evaluation of daily VISEA\_ET with observed  
491 ET, Obv\_ET, at CRO and WET, the bias mainly come from the bias in ERA5\_Rd (the third highest  
492 RMSE of  $45.2 \text{ W m}^{-2}$  and second highest RMSE of  $59.4 \text{ W m}^{-2}$ ) (Fig. 3, a and l). In ENF, the biases  
493 primarily could be by the disability of VISEA\_ET to capturing the Obv\_ET under a cold climate, with low  
494 net radiation estimation (Fig. 5, f), and air temperature (Fig. 4, f). For OSH, the bias mainly arises from  
495 the poor estimation of VISEA\_Rn, which has the lowest NSE of 0.16 and highest RMSE of  $56 \text{ W m}^{-2}$   
496 (Fig. 5, i). The bias of VISEA\_ET in SAV is a result of the combined biases in ERA5\_Rd (the lowest  
497 NSE and R of 0.29 and 0.59, respectively, and the highest RMSE of  $63.2 \text{ W m}^{-2}$ ), VISEA\_Ta (the second  
498 lowest NSE and R of -0.19 and 0.57, respectively).

499

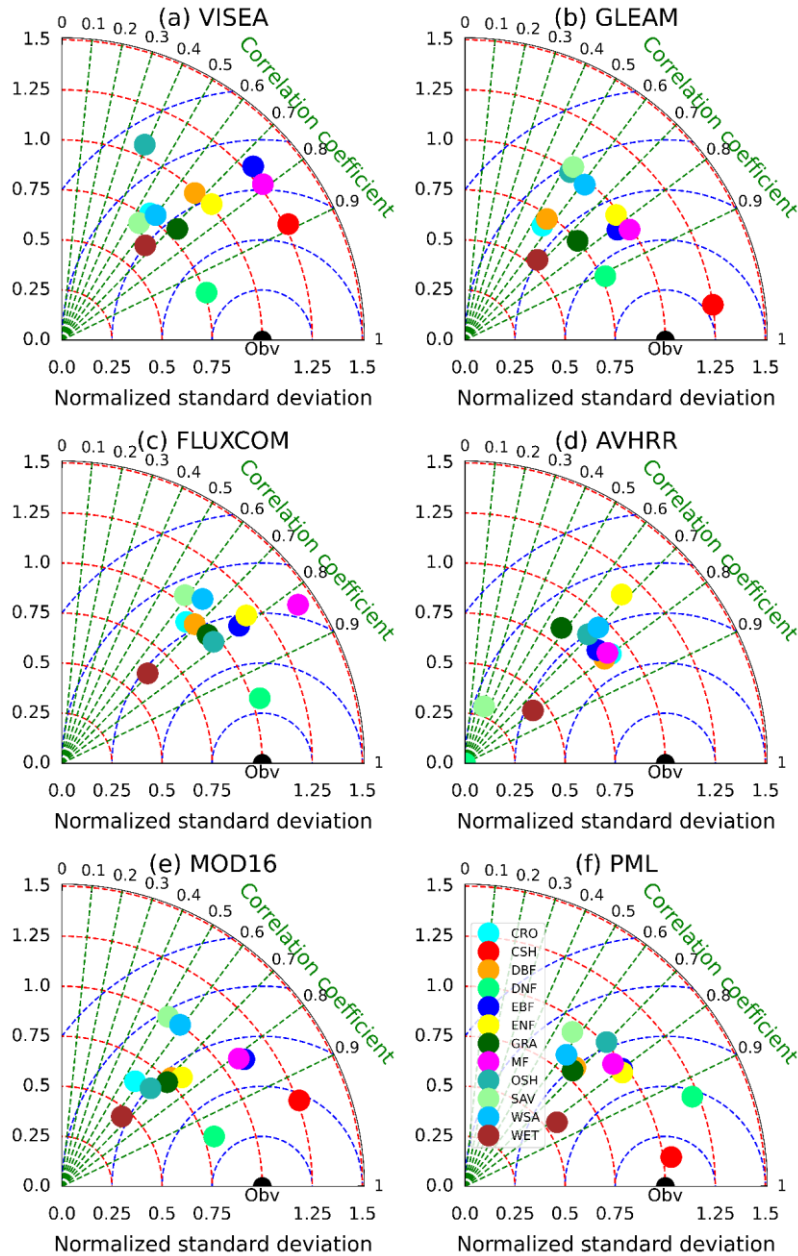
500



501

502 **Figure 6.** The scatter plot of daily ET simulated by VISEA (VISEA\_ET) compared with local instruments  
 503 measurements (Obsv\_ET) under 12 IGBP land cover types: CRO (Croplands), CSH (Closed shrublands),  
 504 DBF (Deciduous broadleaf forests), DNF (Deciduous needle leaf forests), EBF (Evergreen broadleaf  
 505 forests), ENF (Evergreen needle leaf forests), GRA (Grasslands), MF (Mixed forests), OSH (Open  
 506 shrublands), SAV (Savannas), WSA (Woody savannas), WET (Permanent wetlands). The red dotted line  
 507 is the 1:1 line. N is the number of data points, NSE is Nash-Sutcliffe Efficiency, R is correlation  
 508 coefficients, RMSE is Root Mean Square Error, RMSEs is systematic RMSE, and RMSEu is  
 509 unsystematic RMSE. The frequency denotes the probability density estimated through the Kernel Density  
 510 Estimation, KDE method with a Gaussian kernel, and it is then scaled to ensure that the maximum value  
 511 of the probability density function equals 1.

512 In Figure 7, we utilized Taylor diagrams (Taylor, 2001) to evaluate the performances of six global  
 513 gridded monthly ET products with simulated ET from VISEA (a), GLEAM (b), FLUXCOM (c), AVHRR  
 514 (d), MOD16 (e), and PML (f). Table 3 lists statistical metrics including correlation coefficient (CC), bias,  
 515 RMSE, RMSEu, RMSEs, and Nash-Sutcliffe Efficiency (NSE) across different vegetation types and their  
 516 mean values. The vegetation types include Croplands (CRO), Closed Shrublands (CSH), Deciduous  
 517 Broadleaf Forest (DBF), Deciduous Needleleaf Forest (DNF), Evergreen Broadleaf Forest (EBF),  
 518 Evergreen Needleleaf Forest (ENF), Grasslands (GRA), Mixed Forests (MF), Open Shrublands (OSH),  
 519 Savannas (SAV), Woody Savannas (WSA), Wetlands (WET), and an overall mean (MEAN).



520

521 **Figure 7.** Taylor Diagrams comparing monthly measurements of (a) VISEA, GLEAM (b), FLUXCOM  
 522 (c), AVHRR (d), MOD16 (e), and PML (f) with 150 flux towers (labeled as Obv) in different IGBP land  
 523 cover types. The diagrams display the Normalized Standard Deviation (represented by red circles),  
 524 Correlation Coefficient (shown as green lines), and Centred Root-Mean-Square (depicted as blue circles).

525 **Table 3.** Statistical variables of six ET Products – CC (Correlation Coefficient), Ratio (the ratio of the  
526 standard deviations of simulated ET and flux tower measurements), Bias, RMSE, RMSEu, RMSEs, and  
527 NSE.

		CRO	CSH	DBF	DNF	EBF	ENF	GRA	MF	OSH	SAV	WSA	WET	MEAN
<b>WISEA</b>	CC	0.57	0.89	0.67	0.95	0.74	0.74	0.72	0.79	0.39	0.55	0.6	0.66	0.69
	Ratio	0.77	1.27	0.99	0.76	1.29	1.01	0.8	1.27	1.06	0.7	0.78	0.63	0.94
	Bias	-14.16	-1.27	3.9	-19.06	1.37	-12.84	-13.47	1.53	-6.83	-0.45	-23.14	-31.98	-9.70
	RMSE	39.4	12.5	34	22.1	30.4	28.5	32	23.3	30.4	32.5	41.2	51.6	31.49
	RMSEU	27.4	12.1	30.7	7.4	30.4	23.8	23.1	23.2	25.4	22.5	25.8	25.4	23.10
	RMSES	28.3	3.1	14.5	20.8	2.2	15.7	22.2	1.5	16.8	23.5	32.1	44.9	18.80
	NSE	0.18	0.64	0.34	0.45	0.24	0.33	0.41	0.38	-0.36	0.28	0.01	0.08	0.25
<b>GLEAM</b>	CC	0.56	0.99	0.56	0.91	0.81	0.77	0.75	0.83	0.53	0.53	0.61	0.67	0.71
	Ratio	0.69	1.25	0.73	0.77	0.94	0.98	0.75	0.99	0.99	1.02	0.98	0.54	0.89
	Bias	-5.68	10.71	3.55	-6.12	3.41	2.34	-2.01	10.67	4.44	-7.99	-17	-16.26	-1.66
	RMSE	36.8	12.1	35.8	14.6	21.4	23.8	27.6	20.2	25.6	38.4	39.8	43.3	28.28
	RMSEU	24.6	3.2	25.4	9.6	19.4	22.0	20.7	16.3	21.9	33.2	31.9	21.4	20.80
	RMSES	27.3	11.6	25.3	10.9	9.1	9	18.2	11.9	13.1	19.3	23.7	37.7	18.09
	NSE	0.29	0.60	0.28	0.77	0.62	0.53	0.57	0.53	0.03	-0.01	0.06	0.34	0.38
<b>FLUXCOM</b>	CC	0.66	0.98	0.69	0.95	0.79	0.78	0.75	0.83	0.78	0.59	0.65	0.69	0.76
	Ratio	0.94	1.76	0.96	1.04	1.12	1.18	0.97	1.42	0.97	1.04	1.08	0.62	1.09
	Bias	7.22	23.49	17.57	-2.26	6.29	6.40	6.91	21.02	10.04	0.74	-9.75	-14.04	6.14
	RMSE	35.8	27.9	36.7	9.9	25.2	26.7	30.0	31.9	19.8	35.5	37.8	41.7	29.91
	RMSEU	31.0	5.8	28.9	9.7	24.1	25.8	26.8	23.5	15.8	32.3	34.3	24.2	23.52
	RMSES	18.0	27.3	22.6	2.3	7.5	7	13.4	21.6	11.9	14.8	15.8	33.9	16.34
	NSE	0.32	-1.14	0.23	0.88	0.48	0.42	0.48	-0.17	0.43	0.14	0.17	0.40	0.22
<b>AVHRR</b>	CC	0.8	-	0.8	-	0.76	0.68	0.58	0.79	0.69	0.32	0.7	0.79	0.69
	Ratio	0.91	-	0.87	-	0.87	1.15	0.83	0.9	0.89	0.3	0.95	0.43	0.81
	Bias	-1.15	-	5.96	-	5.24	-2.73	-7.04	0.16	-2.41	-47.83	-0.42	-25.32	-7.55
	RMSE	23.6	-	26.1	-	23.3	31	36	18.8	22.1	54.7	33.2	46.6	31.54
	RMSEU	21.2	-	22	-	19.5	29.8	27.9	16.6	18.8	-	29.8	14.6	22.24
	RMSES	10.4	-	14.1	-	12.7	8.4	22.7	8.7	11.6	54.2	14.6	44.2	20.16
	NSE	0.63	-	0.61	-	0.54	0.23	0.24	0.62	0.43	-2.79	0.42	0.29	0.12
<b>MOD16</b>	CC	0.57	0.94	0.71	0.95	0.82	0.74	0.71	0.81	0.67	0.53	0.59	0.65	0.72
	Ratio	0.64	1.26	0.77	0.8	1.11	0.81	0.74	1.09	0.66	1	1	0.46	0.86
	Bias	-7.88	-14.03	5.79	-4.07	-7.17	-4.51	-5.05	4.09	-6.41	-16.01	-23.76	-21.07	-8.34
	RMSE	36.9	16.7	30.7	11.1	23.4	24.3	29.6	19.4	20.4	40.4	44.3	47.2	28.70
	RMSEU	23	8.4	23	7.4	22	19.3	21.7	18.7	12.8	32.4	33.3	18.8	20.07
	RMSES	28.8	14.4	20.3	8.2	7.8	14.9	20.2	5.2	15.9	24.2	29.1	43.3	19.36
	NSE	0.28	0.24	0.48	0.87	0.55	0.52	0.5	0.57	0.39	0.12	0.14	0.23	0.41
<b>PML</b>	CC	0.68	0.99	0.68	0.93	0.8	0.81	0.68	0.77	0.7	0.57	0.61	0.82	0.75
	Ratio	0.8	1.04	0.81	1.22	0.98	0.97	0.79	0.96	1.01	0.94	0.83	0.56	0.91
	Bias	-6.6	-3	-3.39	0.47	-1.42	-6.07	-6.66	-0.59	6.48	-0.18	-16.04	-22.1	-4.93
	RMSE	33.2	4.1	31.5	13.3	21.9	22.2	31.7	19.8	21.1	34.5	37.5	40.5	25.94
	RMSEU	25.6	2.8	25.1	12.7	20.5	20.1	24.1	18.2	18.6	29.5	27.1	17.3	20.13
	RMSES	21.1	3.1	19	3.9	7.8	9.6	20.6	7.7	9.9	17.8	26	36.6	15.26
	NSE	0.42	0.95	0.44	0.79	0.61	0.6	0.43	0.55	0.33	0.19	0.16	0.43	0.49

528

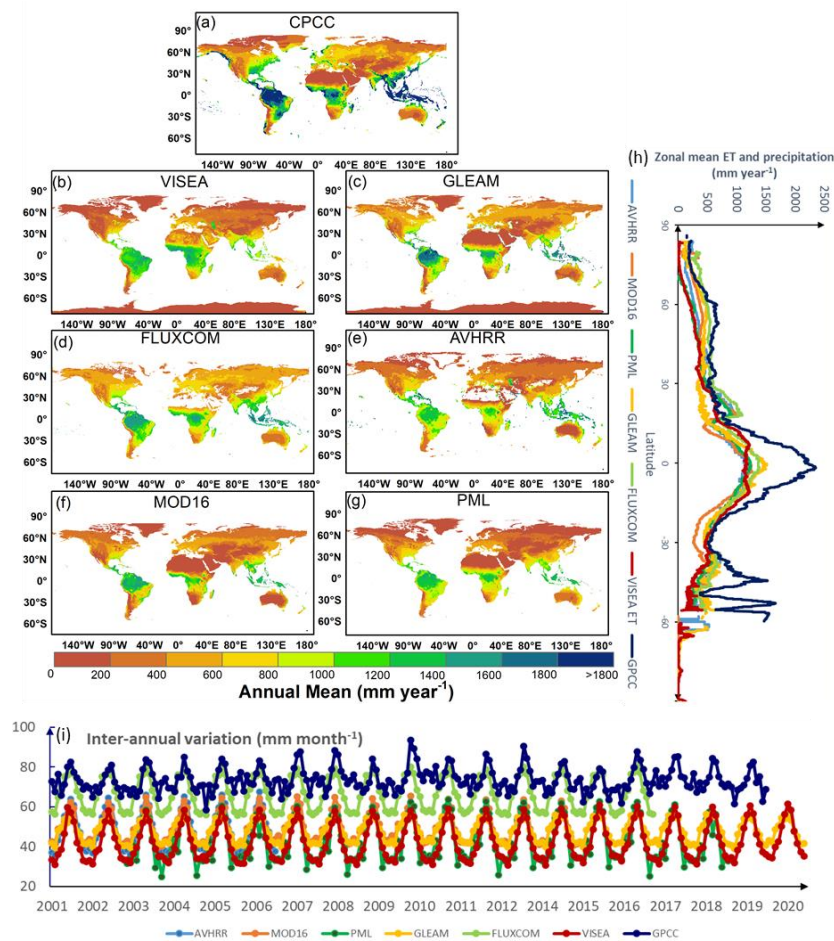
529 VISEA, with a mean correlation coefficient (CC) of 0.69, indicates moderate correlation across  
530 vegetation types but suffers from significant biases, notably in WET, with a mean bias of -9.7 mm month<sup>-1</sup>.  
531 It also has the highest mean Root Mean Square Error (RMSE) at 31.5 mm month<sup>-1</sup> and a mean NSE of  
532 0.25. MOD16 demonstrates a slightly better correlation with a mean CC of 0.72 and presents less  
533 variation in bias, resulting in a marginally lower mean RMSE of 28.7 mm month<sup>-1</sup> and a higher mean  
534 NSE of 0.41. AVHRR matches VISEA in mean CC at 0.69 but exhibits extreme biases, particularly in

535 SAV, and achieves a comparable mean RMSE of 31.5 mm month<sup>-1</sup>. However, its mean NSE of 0.12 is  
 536 the lowest among the six products, suggesting its predictions are less reliable.

537 On the other hand, GLEAM, FLUXCOM, and PML show better agreements. GLEAM has a high  
 538 mean CC of 0.71 with the lowest bias at -1.66 mm month<sup>-1</sup>, indicating a consistent performance with a  
 539 mean RMSE of 28.3 mm month<sup>-1</sup> and a mean NSE of 0.38. FLUXCOM exhibits a higher mean CC of  
 540 0.76, suggesting better overall correlation, but with a higher mean bias of 6.1 mm month<sup>-1</sup>, it hints at a  
 541 tendency towards overestimation. The mean RMSE stands at 29.9 mm month<sup>-1</sup>, with a mean NSE of 0.22.  
 542 PML outperforms the others with the highest mean CC of 0.75 and the highest mean NSE of 0.49,  
 543 indicating the strongest predictive accuracy. It also has the lowest mean RMSE at 25.9 mm month<sup>-1</sup>,  
 544 affirming its status as the most accurate ET estimation product among those evaluated.

545 Figure 8 illustrates the spatial distribution of the multi-year average (a-g), the zonal mean (h) and  
 546 inter-annual variation (i) of (a) GPCC (2001-2019), (b) VISEA (2001-2020), (c) GLEAM (2001-2020),  
 547 (d) FLUXCOM (2001-2016), (e) AVHRR (2001-2006), (f) MOD16 (2001-2014) and (g) PML (2003-  
 548 2018).

549



550

551 **Figure 8.** The spatial distribution of the multi-year average (a-g), the zonal mean (h) and inter-annual  
 552 variation (i) of (a) GPCC (2001-2019), (b) VISEA (2001-2020), (c) GLEAM (2001-2020), (d)  
 553 FLUXCOM (2001-2016), (e) AVHRR (2001-2006), (f) MOD16 (2001-2014) and (g) PML (2003-2018).

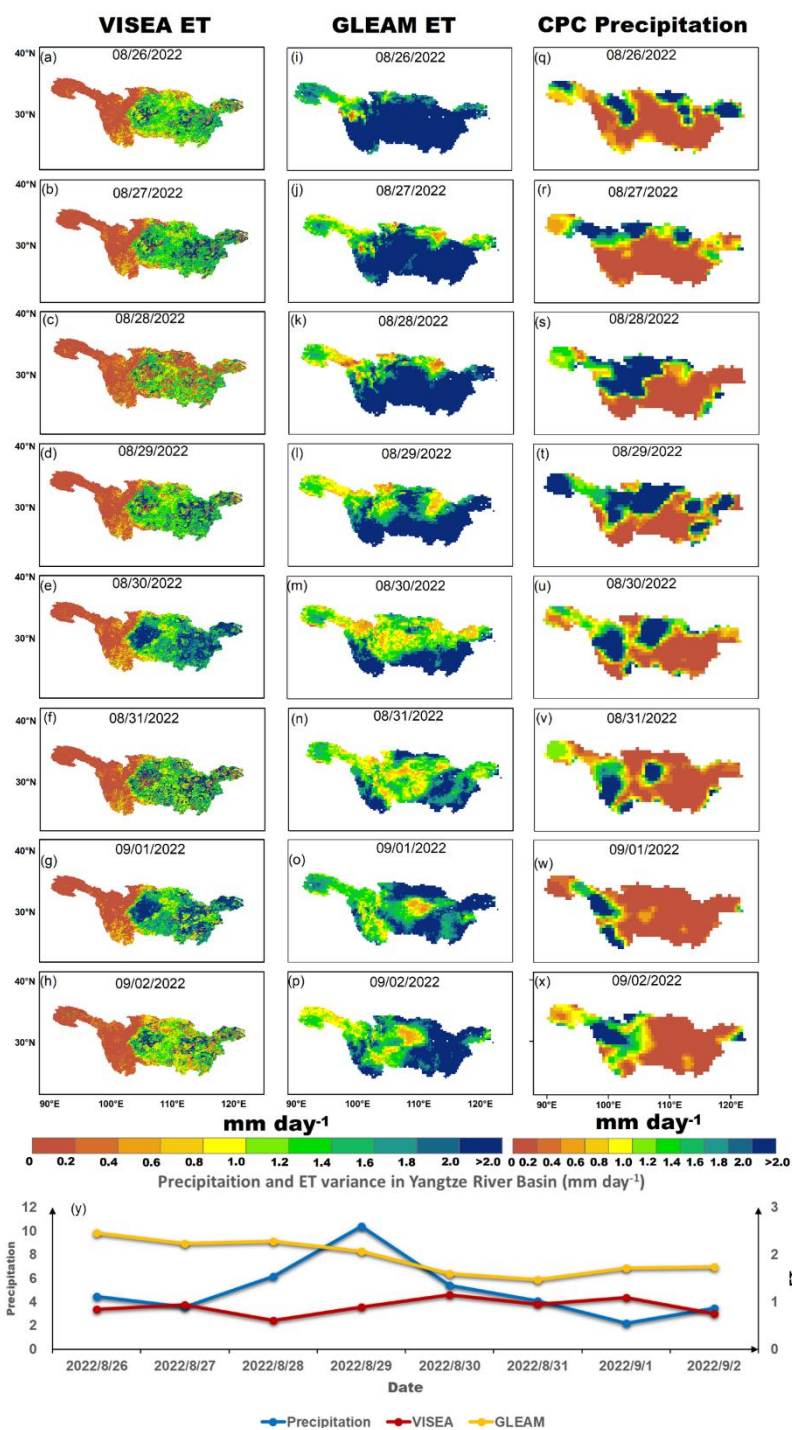
554 The VISEA ET product demonstrates consistent spatial distribution patterns among the six ET  
555 products across various years, both in terms of annual means (a-g) and latitude zonal means (h). These  
556 patterns align closely with the precipitation distribution data from GPCC. It also exhibits similar  
557 distributions to other ET products, both below the 5<sup>th</sup> percentile (Figure S4) and above the 95<sup>th</sup> percentile  
558 (Figure S5). The highest ET values (about 1,500 mm year<sup>-1</sup>) are predominantly concentrated in equatorial  
559 low-latitude regions with the highest precipitation levels (nearly 2,500 mm year<sup>-1</sup>). The available water  
560 for evaporation and transpiration is abundant, and the primary constraint on evapotranspiration lies in the  
561 availability of energy to drive the process. In such conditions, water availability is not a limiting factor,  
562 allowing for ample potential evapotranspiration. These regions include South America (Amazon Basin),  
563 Central Africa (Congo Basin), and Southeast Asia (encompassing Indonesia, Malaysia, parts of Thailand,  
564 and the Philippines), which are known for their tropical rainforest climates. These ET estimates align  
565 with the findings of Chen et al. (2021) and Zhang et al. (2019) who reported that the multi-year average  
566 annual ET is nearly 1,500 and the precipitation is approximately 2,500 mm year<sup>-1</sup> (Panagos et al., 2017).

567 Conversely, areas categorized as barren land (BAR), including deserts such as Sahara, Arabian,  
568 Gobi, Kalahari, and large portions of Australia, as well as snow and ice (SI) areas like most parts of  
569 Canada, Russia, and the Qinghai-Tibet Plateau in China, where the growing seasons are short, typically  
570 falling below 400 mm year<sup>-1</sup>. These areas are also characterized by the lowest annual precipitation,  
571 ranging from 200 to 400 mm year<sup>-1</sup> according to GPCC precipitation data mm year<sup>-1</sup>. ET estimates for  
572 other land cover types fall within this range, varying from 400 to 1,400 mm year<sup>-1</sup>, in close alignment  
573 with the GPCC precipitation data, which falls between 600 to 1,600 mm year<sup>-1</sup>. In these areas, there is a  
574 surplus of available energy, and the primary limitation on ET stems from the availability of water. This  
575 implies a high atmospheric water demand, often quantified as potential evapotranspiration (potential ET).

576 In regions with moisture-limited evapotranspiration (ET), the primary constraint on ET arises from  
577 the limited availability of water. These areas typically experience insufficient precipitation or water  
578 supply, leading to a situation where the atmospheric demand for moisture exceeds the available water  
579 resources. On the other hand, regions with energy-limited ET face limitations due to inadequate energy  
580 for the process of evaporation and transpiration. This can be influenced by factors such as cloud cover,  
581 shading, or other conditions that limit the absorption of solar radiation. In such areas, even if there is an  
582 ample water supply, the lack of sufficient energy hinders the rate of evapotranspiration.

583 Regarding the inter-annual monthly variations, panel (i) shows the fluctuations in ET across different  
584 years for the analyzed ET products and precipitation data. The graph reveals a rhythmic pattern of ET  
585 across the years, VISEA with other ET products showed distinctive peaks and troughs that correspond to  
586 seasonal changes and inter-annual climate variability. The ET products' data exhibit a close alignment  
587 with the precipitation patterns reported by GPCC, highlighting the interconnectedness between ET and  
588 precipitation as climatic variables. Notably, FLUXCOM consistently presents higher ET estimations  
589 compared to the other products, and GLEAM's ET estimations are also slightly higher during the winter,  
590 indicating a trend of systematic overestimation in these products relative to the others in the dataset.

591 Figure 9 presents the daily variations in ET from VISEA and GLEAM along with the precipitation  
 592 from Global Unified Gauge-Based Analysis of Daily Precipitation recorded in the Yangtze River Basin  
 593 during from August 26<sup>th</sup>, 2022, to September 2<sup>nd</sup>, 2022. According to a study by Zhang et al. (2023), the  
 594 Yangtze River Basin endured a significant drought during the summer of 2022, beginning in July and  
 595 showing signs of abatement towards the end of August and into early September. As GLEAM failed to  
 596 capture the variability of ET during this drought and exhibited a negative correlation with precipitation  
 597 data from CPC, we wouldn't discuss it further in this context.



598



599 **Figure 9.** Daily ET from VISEA (a-h), GLEAM (i-p), and CPC precipitation (q-x) distributions  
600 from August 26<sup>th</sup> to September 2<sup>nd</sup> in 2022, alongside daily mean ET and Precipitation variances  
601 in the Yangtze River Basin (y) during the same period.

602 VISEA ET graphically illustrates the evolving drought conditions: with notably low ET levels (below  
603 1 mm day<sup>-1</sup>) across the basin on August 26<sup>th</sup> to 28<sup>th</sup>, evidenced in panel (a-c). A notable increase in  
604 precipitation on August 29<sup>th</sup>, reflected in panels (s) and (u), correlates with an upswing in ET values  
605 (surpassing 1 mm day<sup>-1</sup>) throughout the basin, as visualized in panels (d-f). The graph in panel (y) displays  
606 the variances in mean ET and precipitation within the basin over this timeframe, highlighting a significant  
607 rise in ET (up to 11 mm day<sup>-1</sup>) on August 30<sup>th</sup>, which corresponds with the observed increase precipitation  
608 (reaching 11 mm day<sup>-1</sup>) on August 29<sup>th</sup>.

609 VISEA's ET data align closely with the variances observed in the CPC precipitation data, showcasing  
610 its effectiveness in capturing daily ET fluctuations, especially during and after the drought conditions. It  
611 accurately reflects the dip and subsequent recovery in ET values following the precipitation events,  
612 indicating its robustness in near-real-time monitoring of ET during such hydrological extremes.

## 613 **5. Discussion**

614 While global ET products require at least 2 weeks (GLEAM, FLUXCOM, AVHRR and PML ET  
615 products has more than one years' delay, MOD16 has at least 2 weeks delay) to generate global actual  
616 ET estimation, we developed VISEA, a satellite-based algorithm which is capable of generating near-  
617 real-time evapotranspiration on a daily time step with a resolution of 0.05°. Compared with the monthly  
618 global ET of GLEAM, FLUXCOM, AVHRR which have more than two years' delay and 8-day of  
619 MOD16 and PML which has more than two weeks' delay and also more than one years' delay. This  
620 algorithm is based Nishida et al. (2003) satellite-based evaporation fraction algorithm. To assess its  
621 accuracy, we compared the calculated ET with data from 149 flux towers around the world in various  
622 land use types.

623 Scale mismatch is a problem for many satellite-based ET products. The footprints of these flux towers  
624 typically range from 100 to 200 meters, while the VISEA model outputs gridded cells at a resolution of  
625 0.05° × 0.05° (nearly 25 km<sup>2</sup>). This discrepancy introduces errors, especially since flux towers require a  
626 uniform fetch, which may not represent the larger gridded cell (Sun et al., 2023). To enhance the validity  
627 of our assessments, we assessed monthly values and spatial patterns of our ET measurements with five  
628 other satellite-based ET products named MOD16, AVHRR, GLEAM, FLUXCOM and PML (Figure 7  
629 and 8).

630 The evapotranspiration is calculated with VISEA using shortwave downwards radiation, and  
631 intermediate variables including daily air temperature and net radiation. The calculated  
632 evapotranspiration generally matches local measurements and other model calculated values well but we  
633 found significant biases (Figures 6 and 7). These biases largely arise from inaccuracies in the input ERA5-  
634 Land shortwave radiation (Figure 3), improper application of the VI-Ts method (Figure 4), and  
635 uncertainties in daily net radiation (Figure 5). Below we detail the origin of the biases.

636 Incoming shortwave radiation from ERA5-Land is employed to derive the available energy for  
637 vegetation coverage and bare soil (Eq. 14 and 15), which are the main parameters for calculating daily  
638 ET (Eq. 16). While ERA5-Land is widely utilized as a reanalysis dataset, offering near-real-time land  
639 variables by integrating model data with global observations based on physical laws. However, the  
640 accuracy of shortwave radiation from ERA5-Land seems compromised in savannas (Figure 3) due to the  
641 challenges associated with simulating radiation transmission under land-use changes and aerosol  
642 pollution from natural or anthropogenic sources (Babar et al., 2019; Martens et al., 2020).

643 Air temperature is an important parameter in determining the daily evaporation fraction of bare soil  
644 (Appendix B), canopy surface resistance, aerodynamic resistance of the bare soil (Appendix D) and  
645 atmospheric emissivity (Appendix E), available energy for vegetation coverage and bare soil (Eq. 14 and  
646 15). Since air temperature is not measured directly by satellites, many other ET product use therefore  
647 ground observations, land model or reanalysis data. In contrast, VISEA derives the air temperature from  
648 the negative linear relationship between vegetation index (VI) and surface temperature (Ts) using the VI-  
649 Ts method (section 2.1.3). It gives very good results under grass land, open shrubland and woody  
650 savannas landcover types, as shown in Figure 4. As previously explained, the VI-Ts method relies on the  
651 negative linear correlation between the Vegetation Index (VI) and surface temperature (Ts) within a  $5 \times$   
652  $5$  grid. Therefore, both the variance of VI values across these grid cells and the negative correlation are  
653 essential for calculating the air temperature (Nishida et al., 2003). However, in regions where the  
654 vegetation index and temperature data in adjacent grid cells show small variations, such as dense forests  
655 and bare lands and deserts. Also, in regions with freezing temperatures, the VI-Ts method does perform  
656 well, because warmer temperature is related to increased vegetation, opposite the other regions, where  
657 there is a positive correlation between the vegetation index and surface temperature (Cui et al., 2021).

658 Another bias source of the VISEA model is the uncertainties of daily net radiation, notably originating  
659 from input downward shortwave radiation from ERA5-Land (Figure 2) and VI-Ts estimated air  
660 temperature (Figure 4). The energy budget equation (Eq. 11) and these two figures indicate that net  
661 radiation shows more uncertainties than shortwave radiation and air temperature. At the same time,  
662 assuming a linear relationship between cloud coverage (Eq. 12 and 13) and the calculation of downwards  
663 longwave radiation (Eq. 14 and 15) may be an oversimplification that could introduce uncertainties. Since  
664 available energy for evapotranspiration (ET) depends on net radiation (Eq. 16), addressing these  
665 uncertainties is crucial for enhancing overall model accuracy (Brutsaert, 1975; Huang et al., 2023). Future  
666 refinements will contribute to a more precise daily net radiation estimation within the VISEA model.

667 The VISEA model calculates ET primarily based on vegetation coverage, utilizing it as an indirect  
668 constraint to estimate evapotranspiration. However, this model does not directly incorporate variables  
669 related to water availability, which is a critical factor in ET processes. In tropical regions, where there is  
670 an abundance of solar radiation (available energy), the model tends to overestimate ET due to its emphasis  
671 on vegetation coverage without adequately accounting for the actual water available for  
672 evapotranspiration. This methodology, while effective in capturing the influence of vegetation on ET  
673 under varied conditions, can lead to overestimations in areas where energy availability significantly  
674 exceeds water availability, typical of many tropical regions. Our analysis and subsequent discussion aim

675 to highlight this characteristic of the VISEA model, acknowledging its implications for ET estimations  
676 in such energy-rich, water-variable environments.

677 Furthermore, the VISEA model exhibits a tendency to underestimate ET in colder regions within the  
678 60°N to 90°N latitude range, such as the western territories of Canada. This underestimation is primarily  
679 due to the model's inability to incorporate evaporation from frozen surfaces into its ET calculations. These  
680 discrepancies arise from several factors: inaccuracies in the ERA5-Land shortwave radiation data  
681 (illustrated in Figure 3), the misapplication of the VI-Ts method (explained in Figure 4), and the  
682 uncertainties in daily net radiation (depicted in Figure 5). Designed to amalgamate bare soil and full  
683 vegetation coverage as depicted in Equation 1, the VISEA model encounters difficulties in accurately  
684 estimating ET at higher latitudes, especially in conditions of reduced solar radiation. These challenges  
685 are predominantly linked to the uncertainties associated with ERA5-Land shortwave radiation data,  
686 further compounded by increased cloudiness levels in these regions, as highlighted by Babar et al. (2019).  
687 Such uncertainties have a substantial impact on the model's performance at higher latitudes, affecting its  
688 reliability in these conditions.

689 Despite these challenges, our analysis confirms the VISEA model's ability to provide valuable ET  
690 estimates during the growing season, evidenced by a high Nash-Sutcliffe efficiency (NSE) of 0.4 and a  
691 correlation coefficient (R) of 0.9 when compared against local measurements. These findings support the  
692 model's applicability for ET estimation in the 60°N to 90°N latitude range, highlighting its effectiveness  
693 and relevance during the vegetative growth period.

694 We recognize that variations in the temporal coverage of ET products can introduce variability into  
695 our comparisons. To mitigate this, we have deliberately chosen validation datasets spanning from 2001  
696 to 2020, achieving a uniform analysis timeframe. This selection enabled us to utilize a diverse range of  
697 ET products, effectively minimizing the influence of temporal discrepancies on our comparative analysis.  
698 Concentrating on this two-decade interval has allowed us to robustly evaluate spatial and inter-annual ET  
699 variability, significantly reducing potential biases associated with differing dataset durations. This  
700 method enhances the clarity of our validation approach, solidifies the reliability of our comparisons, and  
701 ensures our analysis accurately reflects long-term ET dynamics.

702 The VISEA ET product provides near-real-time global evapotranspiration (ET) data with a mere one-  
703 week delay and a daily resolution of 0.05 degrees, making it a valuable asset for the research community.  
704 It empowers researchers by providing access to information on land surface water consumption in near-  
705 real-time, which is crucial for monitoring and predicting droughts, and enables decision-makers to make  
706 well-informed choices. This not only enhances research efficiency but also supports more effective and  
707 expedited actions within the scientific and environmental research community.

708 The accuracy of the VISEA model could be enhanced by incorporating additional satellite and climate  
709 data with higher resolution and improved accuracy. Moreover, the delay in providing ET data could be  
710 reduced to three days or less by integrating real-time updated satellite and climate data. In response to  
711 the suggestion to conclude our discussion with specific recommendations for future research directions,

712 we recognize the importance of addressing the identified gaps and uncertainties. We propose exploring  
713 the development of alternative methods for estimating air temperature and net radiation to provide more  
714 accurate and reliable models. Additionally, incorporating variables such as soil moisture and water  
715 availability into the model could further refine its precision. By integrating these suggestions, we aim to  
716 outline a comprehensive roadmap for future research that builds upon our findings, significantly  
717 contributing to the enhancement of environmental modelling and prediction within the field.

## 718 **6. Conclusion**

719 In recent decades, several ET products using satellites have been developed, but few of them  
720 provide near-real-time global terrestrial ET estimates. Despite being updated at the fastest rate, the  
721 MOD16 ET dataset still encounters a delay of more than two weeks. In this study, we provide a satellite-  
722 based near-real-time global daily terrestrial ET estimates by incorporating near-real-time updated hourly  
723 shortwave radiation data from ERA5 and MODIS land products at a spatial resolution of 0.05°. The  
724 assessments indicate that near-real-time ET estimation with VISEA achieves comparable accuracy to  
725 other existing data products and offers a significantly shorter time frame for daily data availability.

726 The new VISEA aligns well with measurements at 149 tower flux sites distributed globally in both  
727 daily and monthly time scales. It demonstrates competitive correlation coefficients and Nash-Sutcliffe  
728 efficiencies (NSEs) across most land cover types but exhibits higher biases. However, like the other five  
729 ET products, it encounters greater uncertainties for the SAV land cover type. In the comparison of the  
730 multiple-year average spatial distribution of other monthly ET products and GPCC precipitation, VISEA  
731 consistently demonstrates spatial patterns aligned with GPCC in most areas, featuring elevated values in  
732 tropical rainforest regions and lower values in arid and semi-arid zones. This alignment underscores  
733 VISEA's proficiency in portraying the spatial distribution of evapotranspiration, offering valuable  
734 insights into water consumption dynamics across diverse geographical regions. However, VISEA  
735 exhibits slightly higher estimates in the Sahara region and lower estimations in the western Canada. In  
736 future studies, the VISA ET algorithm can be enhanced by incorporating more precise models for the  
737 radiation estimation in savanna and the evaporation from the frozen surface. These improvements will  
738 greatly contribute to enhancing the overall accuracy of the algorithm. The satellite-based near-real-time  
739 global daily terrestrial ET estimates could be beneficial for meteorology and hydrology applications  
740 requiring real-time data, especially in coordinating relief efforts during droughts.

## 741 **7. Code Availability**

742 Python code to synthesise the results and to generate the figures of VISEA results and the codes for  
743 generating the global ET products can be obtained through the public repository at  
744 <https://doi.org/10.6084/m9.figshare.24647721.v1> (Huang, 2023c).

## 745 **8. Data Availability**

746 The VISEA ET data can be obtained from <https://data.tpdc.ac.cn/en/data/236e33bf-e66b-4682-bbc1-274de1dcbcd3> (Huang, 2023a).

## 748 **8.1 Input data**

749 MOD11C1 can be obtained at <https://e4ftl01.cr.usgs.gov/MOLT/MOD11C1.061/>. MOD09CMG can be  
750 obtained at <https://e4ftl01.cr.usgs.gov/MOLT/MOD09CMG.061/>. MCD43C3 can be obtained at  
751 <https://e4ftl01.cr.usgs.gov/MOTA/MCD43C3.061/>. MOD13C1 can be obtained at  
752 <https://e4ftl01.cr.usgs.gov/MOLT/MOD13C1.061/>. MCD12C1 can be obtained at  
753 <https://e4ftl01.cr.usgs.gov/MOLT/MOD21C1.061/>. ERA5-Land shortwave radiation data can be  
754 obtained at <https://cds.climate.copernicus.eu/cdsapp#!/dataset/reanalysis-era5-land?tab=form>.

## 755 **8.2 Evaluation data**

756 FLUXNET2015 flux towers data (FLUXNET2015: CC-BY-4.0 33) can be obtained at  
757 <https://fluxnet.org/data/download-data/>. The GLEAM 3.8a ET dataset was obtained from  
758 <https://www.gleam.eu/#downloads> (an email is required to receive a password for the SFTP). The  
759 FLUXCOM ET dataset was freely available (CC4.0 BY licence) from [https://www.fluxcom.org/EF-  
760 Download/](https://www.fluxcom.org/EF-Download/) the Data Portal (an email is required to are receive a password for the FTP). MOD16 ET with  
761 the resolution of 0.05° was freely downloaded from  
762 [http://files.ntsug.umt.edu/data/NTSG\\_Products/MOD16/MOD16A2\\_MONTHLY.MERRA\\_GMAO\\_1k  
763 mALB/Previous/](http://files.ntsug.umt.edu/data/NTSG_Products/MOD16/MOD16A2_MONTHLY.MERRA_GMAO_1kmALB/Previous/). Additionally, the AVHRR ET dataset with 1° was sourced from  
764 [http://files.ntsug.umt.edu/data/ET\\_global\\_monthly\\_ORIG/Global\\_1DegResolution/ASCIIFormat/](http://files.ntsug.umt.edu/data/ET_global_monthly_ORIG/Global_1DegResolution/ASCIIFormat/).  
765 Lastly, the PML ET dataset was obtained from [https://www.tpdc.ac.cn/zh-hans/data/48c16a8d-d307-  
766 4973-abab-972e9449627c](https://www.tpdc.ac.cn/zh-hans/data/48c16a8d-d307-4973-abab-972e9449627c).

767 The precipitation from Global Precipitation Climatology Centre (GPCC) data was as obtained at  
768 [https://cds.climate.copernicus.eu/cdsapp#!/dataset/insitu-gridded-observations-global-and-  
769 regional?tab=form](https://cds.climate.copernicus.eu/cdsapp#!/dataset/insitu-gridded-observations-global-and-regional?tab=form). The precipitation from Global Unified Gauge-Based Analysis of Daily Precipitation  
770 (CPC) was obtained at [https://downloads.psl.noaa.gov/Datasets/cpc\\_global\\_precip/precip.2022.nc](https://downloads.psl.noaa.gov/Datasets/cpc_global_precip/precip.2022.nc)

771 Other data that supports the analysis and conclusions of this work is available at  
772 [https://figshare.com/articles/dataset/Satellite-based\\_Near-Real  
773 Time\\_Global\\_Daily\\_Terrestrial\\_Evapotranspiration\\_Estimates/24669306](https://figshare.com/articles/dataset/Satellite-based_Near-Real_Time_Global_Daily_Terrestrial_Evapotranspiration_Estimates/24669306) (Huang, 2023d).

774

775 **Appendix**

776 **Appendix A. Determining the vegetation fraction calculation:**

777 
$$f_{veg} = \frac{NDVI - NDVI_{min}}{NDVI_{max} - NDVI_{min}} \quad (A1)$$

778 where the  $NDVI$  is the Normalized Difference Vegetation Index and can be calculated as:

779 
$$NDVI = \frac{R_{nir} - R_{red}}{R_{nir} + R_{red}} \quad (A2)$$

780 where  $NDVI_{min}$  is the  $NDVI$  of the bare soil without plants and  $NDVI_{max}$  is the  $NDVI$  of the full  
781 vegetation cover,  $R_{nir}$  is the near-infrared reflectance and  $R_{red}$  is the red reflectance. The daily  
782 reflectance  $R_{nir}$  and  $R_{red}$  were measured by MODIS reflectance data MOD09CMG (Fig. 1). Based on  
783 Tang et al. (2009), we set  $NDVI_{min} = 0.22$  and  $NDVI_{max} = 0.83$ . Missing observation for the daily  
784 MOD09CMG calculated  $NDVI$  data was filled with the 16-day averaged  $NDVI$  values in the  
785 MOD13Q1 data product (Fig. 1).

786

787 **Appendix B. Determining the instantaneous EF:**

788 Combining Eq. 1 and 4, we first calculated the instantaneous evaporation fraction,  $EF^i$  as:

789 
$$EF^i = f_{veg} \frac{Q_{veg}^i}{Q^i} EF_{veg}^i + (1 - f_{veg}) \frac{Q_{soil}^i}{Q^i} EF_{soil}^i \quad (B1)$$

790 where the superscript  $i$  stands for the instantaneous value of the parameter,  $EF_{veg}^i$  and  $EF_{soil}^i$  are the  
 791 instantaneous full vegetation coverage and bare soil  $EF$ , respectively.  $EF_{veg}^i$  can be expressed as a  
 792 function of instantaneously parameters as ( Nishida et al., 2003):

793 
$$EF_{veg}^i = \frac{\alpha \Delta^i}{\Delta^i + \gamma(1 + r_{c\,veg}^i / 2r_{a\,veg}^i)} \quad (B2)$$

794 where  $\alpha$  is the Priestley-Taylor parameter, which was set to 1.26 for wet surfaces (De Bruin, 1983);  $\Delta^i$  is  
 795 the slope of the saturated vapor pressure, which is a function of the temperature (Pa K<sup>-1</sup>);  $\gamma$  is the  
 796 psychrometric constant (Pa K<sup>-1</sup>);  $r_{c\,veg}^i$  is the instantaneous surface resistance of the vegetation canopy (s  
 797 m<sup>-1</sup>);  $r_{a\,veg}^i$  is the instantaneous aerodynamics resistance of the vegetation canopy (s m<sup>-1</sup>).  $EF_{soil}^i$  was  
 798 expressed by Nishida et al. (2003) as a function of the instantaneous soil temperature and the available  
 799 energy based on the energy budget of the bare soil:

800 
$$EF_{soil}^i = \frac{T_{soil\,max}^i - T_{soil}^i}{T_{soil\,max}^i - T_a^i} \frac{Q_{soil0}^i}{Q_{soil}^i} \quad (B3)$$

801 where  $T_{soil\,max}^i$  is the instantaneous maximum possible temperature at the surface reached when the land  
 802 surface is dry (K),  $T_{soil}^i$  is the instantaneous temperature of the bare soil (K),  $T_a^i$  is the instantaneous air  
 803 temperature,  $Q_{soil0}^i$  is the instantaneous available energy when  $T_{soil}^i$  is equal to  $T_a^i$  (W m<sup>-2</sup>).

804

805 **Appendix C. Determining of decoupling factor:**

806  $\Omega_i^*$  is the value of the decoupling factor,  $\Omega$ , for wet surface. According to Pereira (2004),  $\Omega$  and  $\Omega^*$  can  
807 be expressed as:

808

809

810 
$$\Omega = \frac{1}{1 + \frac{\gamma r_c}{\Delta + \gamma r_a}} \quad (C1)$$

811 
$$\Omega^* = \frac{1}{1 + \frac{\gamma r^*}{\Delta + \gamma r_a}} \quad (C2)$$

812 
$$r^* = \frac{(\Delta + \gamma) \rho C_p VPD}{\Delta \gamma (R_n - G)} \quad (C3)$$

813 where  $r_c$  is the surface resistance ( $s\ m^{-1}$ );  $r_a$  is the aerodynamic resistance ( $s\ m^{-1}$ ); the calculation details  
814 of instantaneous and daily  $r_c$  and  $r_a$  for vegetation and soil are explained in Appendix A.  $r^*$  is the critical  
815 surface resistance when the actual evapotranspiration equals the potential evaporation (called equilibrium  
816 evapotranspiration,  $s\ m^{-1}$ );  $\rho$  is the air density ( $kg\ m^{-3}$ );  $C_p$  is the specific heat of the air ( $J\ kg^{-1}\ K^{-1}$ );  $VPD$   
817 is the vapor pressure deficit of the air (Pa).  $\Delta$  is the slope of the saturated vapor pressure ( $Pa\ K^{-1}$ ).

818



819 **Appendix D. Determining the resistances of vegetation canopy and bare soil surface**

820 The canopy surface resistance of the vegetation, denoted as  $r_{c\ veg}$  ( $s\ m^{-1}$ ), was determined using the  
821 relationship established by Jarvis et al. (1976), is equivalent to:

$$822 \quad \frac{1}{r_{c\ veg}} = \frac{f_1(T_a)f_2(PAR)f_3(VPD)f_4(\varphi)f_5(CO_2)}{r_{cMIN}} + \frac{1}{r_{cuticle}} \quad (D1)$$

823 The minimum resistance  $r_{cMIN}$  ( $s\ m^{-1}$ ) is defined as 33 ( $s\ m^{-1}$ ) for cropland and 50 ( $s\ m^{-1}$ ) for forest  
824 as determined by Tang et al. (2009); the canopy resistance related to diffusion through the cuticle layer  
825 of leaves  $r_{cuticle}$  is set at 100,000 ( $s\ m^{-1}$ ) in the Biome-BGC model is according to White et al. (2000).  
826 The relationships involving air temperature  $T_a$ ,  $f_1(T_a)$  and photosynthetic active radiation  $PAR$ ,  $f_2(PAR)$   
827 expressed by the functions provided Jarvis et al. (1976):

$$828 \quad f_1(T_a) = \left( \frac{T_a - T_n}{T_o - T_n} \right) \left( \frac{T_x - T_a}{T_x - T_a} \right)^{\left( \frac{T_x - T_o}{T_o - T_n} \right)} \quad (D2)$$

829 The minimum, optimal, and maximum temperatures for stomatal activity are denoted as  $T_n$ ,  $T_o$  and  
830  $T_x$ , respectively. As per Tang et al. (2009),  $T_n$  is set to 275.85 K,  $T_o$  to 304.25 K, and  $T_x$  to 318.45 K. The  
831 expression for the function  $f_2(PAR)$  is provided below:  
832

$$833 \quad f_2(PAR) = \frac{PAR}{PAR + A} \quad (D3)$$

834 where  $PAR$  is photosynthetic active radiation per unit area and time ( $\mu\ mol\ m^{-2}\ s^{-1}$ ) calculated by  
835 incoming solar radiation multiplied by 2.05 (White et al., 2000);  $A$  is a parameter related to photon  
836 absorption efficiency at low light intensity, which was set to  $152\ \mu\ mol\ m^{-2}\ s^{-1}$  20; Nishida<sup>32</sup> found that  
837 in Eq. D1 the following functions can be omitted without great loss of accuracy: the functions depending  
838 on vapor pressure deficit,  $f_3(VPD)$ , leaf water potential  $f_4(\varphi)$  and carbon dioxide vapor pressure,  
839  $f_5(CO_2)$ .

840 The photosynthetic active radiation per unit area and time ( $PAR$ ), measured in  $\mu\ mol\ m^{-2}\ s^{-1}$ , is  
841 computed by multiplying incoming solar radiation by 2.05, as outlined by White et al. (2000). The  
842 parameter  $A$ , associated with photon absorption efficiency at low light intensity, is established at  $152\ \mu\ mol\ m^{-2}\ s^{-1}$ .  
843 Nishida et al. (2003) observed that, in Eq. D1, the functions tied to vapor pressure deficit  
844  $f_3(VPD)$ , leaf water potential  $f_4(\varphi)$ , and carbon dioxide vapor pressure  $f_5(CO_2)$  can be omitted without  
845 significant loss of accuracy. Tang et al. (2009) employed this canopy resistance approach to estimate  
846 evapotranspiration (ET) at a 500 meter resolution in the Kalam river basin. The evaluation of their results  
847 indicated that the simplification of these calculations did not significantly impact the final accuracy of  
848 ET estimates. Additionally, Huang et al. (2017, 2021, and 2023) evaluated this method for 0.05 degree  
849 ET assessments across China. The evaluation results also demonstrated that the reduction in vapor  
850 pressure deficit (VPD) and leaf water potential had minimal effects on the final ET estimates.

851 The aerodynamic resistance of the canopy, denoted as  $r_{a\ veg}$  ( $s\ m^{-1}$ ), is computed for forest cover,  
 852 grassland, and cropland using the empirical formulae presented by Nishida et al. (2003) for both  
 853 instantaneous and daily values.

$$854 \quad \frac{1}{r_{a\ veg\ (forest)}} = 0.008U_{50m} \quad (D4)$$

855 The wind speed at a height of 50 meters above the canopy ( $U_{50m}$ ) is used to determine the  
 856 aerodynamic resistance for grassland and cropland, as follows:

$$857 \quad \frac{1}{r_{a\ veg\ (grassland\ \&\ cropland)}} = 0.003U_{1m} \quad (D5)$$

858 where  $U_{1m}$  is the wind speed 1m above the canopy ( $m\ s^{-1}$ ). The wind speed as a function of the  
 859 height  $z$ ,  $U(z)$  can be calculated by the logarithm profile of wind. A recent study found that the velocity  
 860 log law does not apply to a stratified atmospheric boundary layer (Cheng et al., 2011). Thus D4 and D5  
 861 are valid under neutral boundary layer conditions. Since  $r_{a\ veg}$  is calculated differently for forests (Eq.  
 862 D4) and grasslands/croplands (Eq. D5), we used the land cover classes from the yearly International  
 863 Geosphere-Biosphere Programme (IGBP) (MCD12C1) to identify the land cover and choice the different  
 864 equation of  $r_{a\ veg}$ .  $U_{50m}$  and  $U_{1m}$  were calculated by the logarithm profile of wind:

$$865 \quad U(z) = U_{shear} \ln \left[ \frac{(z-d)}{z_0} \right] / k \quad (D6)$$

866 where  $U_{shear}$  is the shear velocity ( $m\ s^{-1}$ );  $z$  is the height (m);  $d$  is the surface displacement (m);  $z_0$   
 867 is the roughness length, we followed Nishida et al. (2003), set as 0.005 m for bare soil and 0.01 m for  
 868 grassland;  $k$  is the von Kármán's constant and set as 0.4 following Nishida (Nishida et al., 2003). The  
 869 shear velocity  $U_{shear}$  was calculated as:

$$870 \quad U_{shear} = U_{1m\ soil} \frac{0.4}{\ln \left( \frac{1}{0.005} \right)} \quad (D7)$$

871 where the  $U_{1m\ soil}$  is the wind speed of bare soil at 1 m height ( $m\ s^{-1}$ ), it was calculated as:

$$872 \quad U_{1m\ soil} = 1/0.0015\ r_{a\ soil} \quad (D8)$$

873 The Vegetation Index-surface Temperature (VI-T<sub>s</sub>) diagram (Nishida et al., 2003) can be utilized to  
 874 compute the instantaneous air temperature. This is achieved by utilizing MODIS instantaneous surface  
 875 temperature/emissivity data (MOD11C1) and daily-calculated NDVI as input parameters.

876 The aerodynamic resistance of the bare soil, denoted as  $r_{a\ soil}$  ( $s\ m^{-1}$ ), was determined by Nishida  
 877 et al. (2003). This calculation assumes that the maximum surface temperature of bare soil  $T_{soil\ max}$  (K)  
 878 happens when the sum of latent heat flux and sensible heat flux of the bare soil, referred to as the available  
 879 energy of bare soil  $Q_{soil}$  ( $W\ m^{-2}$ ), is utilized as the sensible heat flux, while the latent heat flux is set to  
 880 zero.

$$881 \quad r_{a\ soil} = \frac{\rho C_p (T_{soil\ max} - T_a)}{Q_{soil}} \quad (D9)$$

882  $r_{a\ soil}$  is the aerodynamic resistance of the bare soil, ( $s\ m^{-1}$ ),  $\rho$  is the air density,  $kg\ m^{-3}$ ;  $C_p$  is the  
883 specific heat of the air, ( $J\ kg^{-1}\ K^{-1}$ );  $T_a$  is the air temperature (K),  $Q_{soil}$  is the available energy of bare soil  
884 ( $W\ m^{-2}$ ).

885 To compute the canopy surface resistance of bare soil, denoted as  $r_{c\ soil}$  ( $s\ m^{-1}$ ), we adhere to the  
886 methodologies outlined in the works of Griend and Owe (1994) and Mu et al. (2007):

$$887 \quad r_{c\ soil} = r_{tot} - r_{a\ soil} \quad (D10)$$

$$888 \quad r_{tot} = \frac{1.0}{\left(\frac{T_a}{293.15}\right)^{1.75} \frac{101300}{P}} * 107.0 \quad (D11)$$

889 The total aerodynamic resistance  $r_{tot}$  ( $s\ m^{-1}$ ) is composed of the aerodynamic resistance over the  
890 bare soil  $r_{a\ soil}$  ( $s\ m^{-1}$ ), with atmospheric pressure  $P$  set at 101,300 Pa.

891

892 **Appendix E. The calculation of atmospheric emissivity for clear sky**

893 As per Brutsaert (1975), the atmospheric emissivity  $\varepsilon_a^d$  for clear sky under standard humidity and  
 894 temperature conditions is

$$895 \quad \varepsilon_a^d = 1.24 \times (e_a^d/T_a^d)^{1/7} \quad (E1)$$

896 where  $e_a^d$  represents the daily water vapor pressure (kPa). To calculate  $e_a^d$ , it is necessary to  
 897 compute the slope of the saturated vapor ( $\Delta$ ) as:

$$898 \quad \Delta = \frac{4098 [0.6108 \exp[\frac{17.27T_a}{(T_a+237.3)}]]}{(T_a+237.3)^2} \quad (E2)$$

899 VPD is the vapor pressure deficit of the air (kPa), which is expressed as:

$$900 \quad \text{VPD} = e^0(T_a) - e_a \quad (E3)$$

$$901 \quad e^0(T_a) = 0.6108 \exp \left[ \frac{17.27T_a}{(T_a+237.3)} \right] \quad (E4)$$

$$902 \quad e_a = e^0(T_{dew}) \quad (E5)$$

$$903 \quad e^0(T_{dew}) = 0.6108 \exp \left[ \frac{17.27T_{dew}}{T_{dew}+237.3} \right] \quad (E6)$$

904 The expression within parentheses denotes the independent variable, where,  $e^0(T_a)$  represents the  
 905 saturation vapor pressure (kPa) at the air temperature  $T_a$  (°C);  $e_a$  is the actual vapor pressure (kPa);  
 906  $e^0(T_{dew})$  is the saturation vapor pressure (kPa) at the dew point temperature  $T_{dew}$  (°C). For forest, water  
 907 surface, and cropland  $T_{dew}$  is set to the minimum air temperature during the day. In arid regions such as  
 908 bare soil and non-irrigated grassland,  $T_{dew}$  may be 2-3 °C lower than  $T_{min}$ . Therefore, 2 °C is subtracted  
 909 is subtracted from  $T_{min}$  in arid and semiarid areas to derive  $T_{dew}$ . While these simplifications might  
 910 introduce a bias in the final calculated ET value, our initial results indicate that the effect is negligible.

911

912 **Acknowledgements**

913 This study is supported by the National Key Research and Development Program of China  
914 (No.2017YFA0603703). We employed ChatGPT3.5 to enhance the quality of our English writing and  
915 grammar.

916 **Author contributions**

917 L. H. had the original idea and drafted the paper with help from Y. L.; J. M. C. Q. T., T. S., W. C. and  
918 W. S. participated in the discussion and the many manuscript revisions.

919 **Competing interests**

920 The authors declare no competing interests.

921 **References**

922 Aschonitis, V., Touloumidis, D., ten Veldhuis, M.-C., and Coenders-Gerrits, M.: Correcting  
923 Thornthwaite potential evapotranspiration using a global grid of local coefficients to support  
924 temperature-based estimations of reference evapotranspiration and aridity indices, *Earth System  
925 Science Data*, 14, 163–177, <https://doi.org/10.5194/essd-14-163-2022>, 2022.

926 Awada, H., Di Prima, S., Sirca, C., Giadrossich, F., Marras, S., Spano, D., and Pirastru, M.: A remote  
927 sensing and modeling integrated approach for constructing continuous time series of daily actual  
928 evapotranspiration, *Agricultural Water Management*, 260, 107320,  
929 <https://doi.org/10.1016/j.agwat.2021.107320>, 2022.

930 Babar, B., Graversen, R., and Boström, T.: Solar radiation estimation at high latitudes: Assessment  
931 of the CMSAF databases, ASR and ERA5, *Solar Energy*, 182, 397–411,  
932 <https://doi.org/10.1016/j.solener.2019.02.058>, 2019.

933 Baldocchi, D., Falge, E., Gu, L., Olson, R., Hollinger, D., Running, S., Anthoni, P., Bernhofer, C.,  
934 Davis, K., Evans, R., Fuentes, J., Goldstein, A., Katul, G., Law, B., Lee, X., Malhi, Y., Meyers, T.,  
935 Munger, W., Oechel, W., U, K. T. P., Pilegaard, K., Schmid, H. P., Valentini, R., Verma, S., Vesala,  
936 T., Wilson, K., and Wofsy, S.: FLUXNET: A New Tool to Study the Temporal and Spatial Variability  
937 of Ecosystem-Scale Carbon Dioxide, Water Vapor, and Energy Flux Densities, *Bulletin of the  
938 American Meteorological Society*, 82, 2415–2434, [https://doi.org/10.1175/1520-0477\(2001\)082<2415:FANTTS>2.3.CO;2](https://doi.org/10.1175/1520-0477(2001)082<2415:FANTTS>2.3.CO;2), 2001.

940 Barrios, J. M., Ghilain, N., Arboleda, A., and Gellens-Meulenberghs, F.: Retrieving daily  
941 evapotranspiration from the combination of geostationary and polar-orbit satellite data, in: 2015 8th  
942 International Workshop on the Analysis of Multitemporal Remote Sensing Images (Multi-Temp),  
943 2015 8th International Workshop on the Analysis of Multitemporal Remote Sensing Images (Multi-  
944 Temp), 1–4, <https://doi.org/10.1109/Multi-Temp.2015.7245797>, 2015.

945 Becker, A., Finger, P., Meyer-Christoffer, A., Rudolf, B., Schamm, K., Schneider, U., and Ziese, M.:  
946 A description of the global land-surface precipitation data products of the Global Precipitation  
947 Climatology Centre with sample applications including centennial (trend) analysis from 1901–  
948 present, *Earth System Science Data*, 5, 71–99, <https://doi.org/10.5194/essd-5-71-2013>, 2013.

949 Brutsaert, W.: On a derivable formula for long-wave radiation from clear skies, *Water Resources  
950 Research*, 11, 742–744, <https://doi.org/10.1029/WR011i005p00742>, 1975.

951 Chang, K. and Zhang, Q.: Modeling of downward longwave radiation and radiative cooling potential

- 952 in China, *Journal of Renewable and Sustainable Energy*, 11, 066501,  
953 <https://doi.org/10.1063/1.5117319>, 2019.
- 954 Chen, X., Su, Z., Ma, Y., Trigo, I., and Gentile, P.: Remote Sensing of Global Daily  
955 Evapotranspiration based on a Surface Energy Balance Method and Reanalysis Data, *Journal of*  
956 *Geophysical Research: Atmospheres*, 126, e2020JD032873, <https://doi.org/10.1029/2020JD032873>,  
957 2021.
- 958 Cheng, L., Xu, Z., Wang, D., and Cai, X.: Assessing interannual variability of evapotranspiration at  
959 the catchment scale using satellite-based evapotranspiration data sets, *Water Resources Research*,  
960 47, <https://doi.org/10.1029/2011WR010636>, 2011.
- 961 Copernicus Climate Change Service: Crop productivity and evapotranspiration indicators from 2000  
962 to present derived from satellite observations, <https://doi.org/10.24381/CDS.B2F6F9F6>, 2020.
- 963 Cui, Y., Jia, L., and Fan, W.: Estimation of actual evapotranspiration and its components in an  
964 irrigated area by integrating the Shuttleworth-Wallace and surface temperature-vegetation index  
965 schemes using the particle swarm optimization algorithm, *Agricultural and Forest Meteorology*, 307,  
966 108488, <https://doi.org/10.1016/j.agrformet.2021.108488>, 2021.
- 967 De Bruin, H. a. R.: A Model for the Priestley-Taylor Parameter  $\alpha$ , *J. Climate Appl. Meteor.*, 22, 572–  
968 578, [https://doi.org/10.1175/1520-0450\(1983\)022<0572:AMFTPT>2.0.CO;2](https://doi.org/10.1175/1520-0450(1983)022<0572:AMFTPT>2.0.CO;2), 1983.
- 969 Didan, K.: MOD13C1 MODIS/Terra Vegetation Indices 16-Day L3 Global 0.05Deg CMG V006  
970 [Data set], <https://doi.org/10.5067/MODIS/MOD13C1.006>, n.d.
- 971 Fisher, J. B., Lee, B., Purdy, A. J., Halverson, G. H., Dohlen, M. B., Cawse-Nicholson, K., Wang,  
972 A., Anderson, R. G., Aragon, B., Arain, M. A., Baldocchi, D. D., Baker, J. M., Barral, H., Bernacchi,  
973 C. J., Bernhofer, C., Biraud, S. C., Bohrer, G., Brunsell, N., Cappelaere, B., Castro-Contreras, S.,  
974 Chun, J., Conrad, B. J., Cremonese, E., Demarty, J., Desai, A. R., De Ligne, A., Foltýnová, L.,  
975 Goulden, M. L., Griffis, T. J., Grünwald, T., Johnson, M. S., Kang, M., Kelbe, D., Kowalska, N.,  
976 Lim, J.-H., Maïnassara, I., McCabe, M. F., Missik, J. E. C., Mohanty, B. P., Moore, C. E., Morillas,  
977 L., Morrison, R., Munger, J. W., Posse, G., Richardson, A. D., Russell, E. S., Ryu, Y., Sanchez-  
978 Azofeifa, A., Schmidt, M., Schwartz, E., Sharp, I., Šigut, L., Tang, Y., Hulley, G., Anderson, M.,  
979 Hain, C., French, A., Wood, E., and Hook, S.: ECOSTRESS: NASA's Next Generation Mission to  
980 Measure Evapotranspiration From the International Space Station, *Water Resources Research*, 56,  
981 e2019WR026058, <https://doi.org/10.1029/2019WR026058>, 2020.
- 982 Friedl, M., D. Sulla-Menashe.: MCD12C1 MODIS/Terra+Aqua Land Cover Type Yearly L3 Global  
983 0.05Deg CMG V006 [Data set], <https://doi.org/10.5067/MODIS/MCD12C1.006>, 2015.
- 984 Fritschen, L. J. and Gay, L. W.: Soil Heat Flux, in: *Environmental Instrumentation*, edited by:  
985 Fritschen, L. J. and Gay, L. W., Springer, New York, NY, 86–92, [https://doi.org/10.1007/978-1-4612-6205-3\\_4](https://doi.org/10.1007/978-1-4612-6205-3_4), 1979.
- 987 Goforth, M. A., Gilchrist, G. W., and Sirianni, J. D.: Cloud effects on thermal downwelling sky  
988 radiance, in: *Thermosense XXIV*, 203–213, <https://doi.org/10.1117/12.459570>, 2002.
- 989 Griend, A. A. van de and Owe, M.: Bare soil surface resistance to evaporation by vapor diffusion  
990 under semiarid conditions, *Water Resources Research*, 30, 181–188,  
991 <https://doi.org/10.1029/93WR02747>, 1994.
- 992 Halverson, G. H., Fisher, J., Jewell, L. A., Moore, G., Verma, M., McDonald, T., Kim, S., and Muniz,  
993 A.: Near Real-Time Monitoring of Global Evapotranspiration and its Application to Water Resource  
994 Management, 2016, H54D-01, 2016.
- 995 Han, C., Ma, Y., Wang, B., Zhong, L., Ma, W., Chen, X., and Su, Z.: Long-term variations in actual  
996 evapotranspiration over the Tibetan Plateau, *Earth System Science Data*, 13, 3513–3524,

- 997 <https://doi.org/10.5194/essd-13-3513-2021>, 2021.
- 998 He, S., Zhang, Y., Ma, N., Tian, J., Kong, D., and Liu, C.: A daily and 500&thinspm coupled  
 999 evapotranspiration and gross primary production product across China during 2000–2020, *Earth*  
 1000 *System Science Data*, 14, 5463–5488, <https://doi.org/10.5194/essd-14-5463-2022>, 2022.
- 1001 Huang, L.: Satellite-based Near-Real-Time Global Terrestrial Evapotranspiration Estimation Dataset,  
 1002 [https://doi.org/.](https://doi.org/) <https://doi.org/10.11888/Terre.tpd.300782>  
 1003 <https://cstr.cn/18406.11.Terre.tpd.300782> ., 2023.
- 1004 Huang, L., Li, Z., Tang, Q., Zhang, X., Liu, X., and Cui, H.: Evaluation of satellite-based  
 1005 evapotranspiration estimates in China, *JARS*, 11, 026019, <https://doi.org/10.1117/1.JRS.11.026019>,  
 1006 2017.
- 1007 Huang, L., Steenhuis, T. S., Luo, Y., Tang, Q., Tang, R., Zheng, J., Shi, W., and Qiao, C.: Revisiting  
 1008 Daily MODIS Evapotranspiration Algorithm Using Flux Tower Measurements in China, *Earth and*  
 1009 *Space Science*, 8, e2021EA001818, <https://doi.org/10.1029/2021EA001818>, 2021.
- 1010 Huang, L., Luo, Y., Steenhuis, T., Tang, Q., Cheng, W., Shi, W., Xia, X., Zhao, D., and Liao, Z.: An  
 1011 Improved Satellite-Based Evapotranspiration Procedure for China, *Earth and Space Science*, 10,  
 1012 e2023EA002949, <https://doi.org/10.1029/2023EA002949>, 2023.
- 1013 Idso, S. B., Aase, J. K., and Jackson, R. D.: Net radiation — soil heat flux relations as influenced by  
 1014 soil water content variations, *Boundary-Layer Meteorol*, 9, 113–122,  
 1015 <https://doi.org/10.1007/BF00232257>, 1975.
- 1016 Jarvis, P. G., Monteith, J. L., and Weatherley, P. E.: The interpretation of the variations in leaf water  
 1017 potential and stomatal conductance found in canopies in the field, *Philosophical Transactions of the*  
 1018 *Royal Society of London. B, Biological Sciences*, 273, 593–610,  
 1019 <https://doi.org/10.1098/rstb.1976.0035>, 1976.
- 1020 Jiang, H., Yang, Y., Bai, Y., and Wang, H.: Evaluation of the Total, Direct, and Diffuse Solar  
 1021 Radiations From the ERA5 Reanalysis Data in China, *IEEE Geoscience and Remote Sensing Letters*,  
 1022 17, 47–51, <https://doi.org/10.1109/LGRS.2019.2916410>, 2020.
- 1023 Jung, M.: FLUXCOM Global Land Energy Fluxes,  
 1024 [https://doi.org/10.17871/FLUXCOM\\_EnergyFluxes\\_v1](https://doi.org/10.17871/FLUXCOM_EnergyFluxes_v1), 2018.
- 1025 Jung, M., Reichstein, M., and Bondeau, A.: Towards global empirical upscaling of FLUXNET eddy  
 1026 covariance observations: validation of a model tree ensemble approach using a biosphere model,  
 1027 *Biogeosciences*, 6, 2001–2013, <https://doi.org/10.5194/bg-6-2001-2009>, 2009.
- 1028 Jung, M., Reichstein, M., Ciais, P., Seneviratne, S. I., Sheffield, J., Goulden, M. L., Bonan, G.,  
 1029 Cescatti, A., Chen, J., de Jeu, R., Dolman, A. J., Eugster, W., Gerten, D., Gianelle, D., Gobron, N.,  
 1030 Heinke, J., Kimball, J., Law, B. E., Montagnani, L., Mu, Q., Mueller, B., Oleson, K., Papale, D.,  
 1031 Richardson, A. D., Rouspard, O., Running, S., Tomelleri, E., Viovy, N., Weber, U., Williams, C.,  
 1032 Wood, E., Zaehle, S., and Zhang, K.: Recent decline in the global land evapotranspiration trend due  
 1033 to limited moisture supply, *Nature*, 467, 951–954, <https://doi.org/10.1038/nature09396>, 2010.
- 1034 Jung, M., Koirala, S., Weber, U., Ichii, K., Gans, F., Camps-Valls, G., Papale, D., Schwalm, C.,  
 1035 Tramontana, G., and Reichstein, M.: The FLUXCOM ensemble of global land-atmosphere energy  
 1036 fluxes, *Sci Data*, 6, 1–14, <https://doi.org/10.1038/s41597-019-0076-8>, 2019.
- 1037 Kondo Junsei: *Atmospheric Science near the Ground Surface*, University of Tokyo Press, Tokyo,  
 1038 324 pp., 2000.
- 1039 Martens, B., Miralles, D. G., Lievens, H., van der Schalie, R., de Jeu, R. A. M., Fernández-Prieto,  
 1040 D., Beck, H. E., Dorigo, W. A., and Verhoest, N. E. C.: GLEAM v3: satellite-based land evaporation

- 1041 and root-zone soil moisture, *Geoscientific Model Development*, 10, 1903–1925,  
1042 <https://doi.org/10.5194/gmd-10-1903-2017>, 2017.
- 1043 Martens, B., Schumacher, D. L., Wouters, H., Muñoz-Sabater, J., Verhoest, N. E. C., and Miralles,  
1044 D. G.: Evaluating the land-surface energy partitioning in ERA5, *Geoscientific Model Development*,  
1045 13, 4159–4181, <https://doi.org/10.5194/gmd-13-4159-2020>, 2020.
- 1046 Martin Jung, Sujan Koirala, Ulrich Weber, Kazuhito Ichii, Fabian Gans, Gustau Camps-Valls, Dario  
1047 Papale, Christopher Schwalm, Gianluca tramontana & Markus Reichstein: FLUXCOM Global Land  
1048 Energy Fluxes, [https://doi.org/10.17871/FLUXCOM\\_EnergyFluxes\\_v1](https://doi.org/10.17871/FLUXCOM_EnergyFluxes_v1), 2018.
- 1049 Miralles, D. G., Holmes, T. R. H., De Jeu, R. a. M., Gash, J. H., Meesters, A. G. C. A., and Dolman,  
1050 A. J.: Global land-surface evaporation estimated from satellite-based observations, *Hydrology and  
1051 Earth System Sciences*, 15, 453–469, <https://doi.org/10.5194/hess-15-453-2011>, 2011.
- 1052 Mu, Q., Heinsch, F. A., Zhao, M., and Running, S. W.: Development of a global evapotranspiration  
1053 algorithm based on MODIS and global meteorology data, *Remote Sensing of Environment*, 111,  
1054 519–536, <https://doi.org/10.1016/j.rse.2007.04.015>, 2007.
- 1055 Mu, Q., Zhao, M., and Running, S. W.: Improvements to a MODIS global terrestrial  
1056 evapotranspiration algorithm, *Remote Sensing of Environment*, 115, 1781–1800,  
1057 <https://doi.org/10.1016/j.rse.2011.02.019>, 2011.
- 1058 Mu, Q., Zhao, M., Kimball, J. S., McDowell, N. G., and Running, S. W.: A Remotely Sensed Global  
1059 Terrestrial Drought Severity Index, *Bulletin of the American Meteorological Society*, 94, 83–98,  
1060 <https://doi.org/10.1175/BAMS-D-11-00213.1>, 2013.
- 1061 Muñoz Sabater, J.: ERA5-Land hourly data from 1950 to present., [https://doi.org/DOI:  
1062 10.24381/cds.e2161bac](https://doi.org/DOI:10.24381/cds.e2161bac), 2019.
- 1063 Naud, C. M., Booth, J. F., and Genio, A. D. D.: Evaluation of ERA-Interim and MERRA Cloudiness  
1064 in the Southern Ocean, *Journal of Climate*, 27, 2109–2124, [https://doi.org/10.1175/JCLI-D-13-  
00432.1](https://doi.org/10.1175/JCLI-D-13-<br/>1065 00432.1), 2014.
- 1066 Nishida, K., Nemani, R. R., Running, S. W., and Glassy, J. M.: An operational remote sensing  
1067 algorithm of land surface evaporation, *Journal of Geophysical Research: Atmospheres*, 108,  
1068 <https://doi.org/10.1029/2002JD002062>, 2003.
- 1069 Panagos, P., Borrelli, P., Meusburger, K., Yu, B., Klik, A., Yang, J., Ni, J., Chattopadhyay, N.,  
1070 Sadeghi, S. H., Hazbavi, Z., Zabihi, M., Larionov, G., Krasnov, S., Gorobets, A., Levi, Y., Erpul, G.,  
1071 Birkel, C., and Ballabio, C.: Global rainfall erosivity assessment based on high-temporal resolution  
1072 rainfall records, *Scientific Reports*, 7, <https://doi.org/10.1038/s41598-017-04282-8>, 2017.
- 1073 Pastorello, G., Trotta, C., Canfora, E., Chu, H., Christianson, D., Cheah, Y.-W., Poindexter, C., Chen,  
1074 J., Elbashandy, A., Humphrey, M., Isaac, P., Polidori, D., Reichstein, M., Ribeca, A., van Ingen, C.,  
1075 Vuichard, N., Zhang, L., Amiro, B., Ammann, C., Arain, M. A., Ardö, J., Arkebauer, T., Arndt, S. K.,  
1076 Arriga, N., Aubinet, M., Aurela, M., Baldocchi, D., Barr, A., Beamesderfer, E., Marchesini, L. B.,  
1077 Bergeron, O., Beringer, J., Bernhofer, C., Berveiller, D., Billesbach, D., Black, T. A., Blanken, P. D.,  
1078 Bohrer, G., Boike, J., Bolstad, P. V., Bonal, D., Bonnefond, J.-M., Bowling, D. R., Bracho, R.,  
1079 Brodeur, J., Brümmer, C., Buchmann, N., Burban, B., Burns, S. P., Buysse, P., Cale, P., Cavagna,  
1080 M., Cellier, P., Chen, S., Chini, I., Christensen, T. R., Cleverly, J., Collalti, A., Consalvo, C., Cook,  
1081 B. D., Cook, D., Coursolle, C., Cremonese, E., Curtis, P. S., D'Andrea, E., da Rocha, H., Dai, X.,  
1082 Davis, K. J., Cinti, B. D., Grandcourt, A. de Ligne, A. D., De Oliveira, R. C., Delpierre, N., Desai,  
1083 A. R., Di Bella, C. M., Tommasi, P. di, Dolman, H., Domingo, F., Dong, G., Dore, S., Duce, P.,  
1084 Dufrière, E., Dunn, A., Dušek, J., Eamus, D., Eichelmann, U., ElKhidir, H. A. M., Eugster, W.,  
1085 Ewenz, C. M., Ewers, B., Famulari, D., Fares, S., Feigenwinter, I., Feitz, A., Fensholt, R., Filippa,  
1086 G., Fischer, M., Frank, J., Galvagno, M., et al.: The FLUXNET2015 dataset and the ONEFlux  
1087 processing pipeline for eddy covariance data, *Sci Data*, 7, 225, <https://doi.org/10.1038/s41597-020->



- 1088 0534-3, 2020.
- 1089 Pereira, A. R.: The Priestley–Taylor parameter and the decoupling factor for estimating reference  
1090 evapotranspiration, *Agricultural and Forest Meteorology*, 125, 305–313,  
1091 <https://doi.org/10.1016/j.agrformet.2004.04.002>, 2004.
- 1092 Schaaf, C., Wang, Z: MCD43C1 MODIS/Terra+Aqua BRDF/AlbedoModel Parameters Daily L3  
1093 Global 0.05Deg CMG V006 [Data set], <https://doi.org/10.5067/MODIS/MCD43C1.006>, 2015.
- 1094 Schneider, U., Becker, A., Finger, P., Meyer-Christoffer, A., Ziese, M., and Rudolf, B.: GPCP’s new  
1095 land surface precipitation climatology based on quality-controlled in situ data and its role in  
1096 quantifying the global water cycle, *Theor Appl Climatol*, 115, 15–40,  
1097 <https://doi.org/10.1007/s00704-013-0860-x>, 2014.
- 1098 Schneider, U., Finger, P., Meyer-Christoffer, A., Rustemeier, E., Ziese, M., and Becker, A.:  
1099 Evaluating the Hydrological Cycle over Land Using the Newly-Corrected Precipitation Climatology  
1100 from the Global Precipitation Climatology Centre (GPCP), *Atmosphere*, 8, 52,  
1101 <https://doi.org/10.3390/atmos8030052>, 2017.
- 1102 Su, B., Huang, J., Mondal, S. K., Zhai, J., Wang, Y., Wen, S., Gao, M., Lv, Y., Jiang, S., Jiang, T.,  
1103 and Li, A.: Insight from CMIP6 SSP-RCP scenarios for future drought characteristics in China,  
1104 *Atmospheric Research*, 105375, <https://doi.org/10.1016/j.atmosres.2020.105375>, 2020.
- 1105 Sun, S., Bi, Z., Xiao, J., Liu, Y., Sun, G., Ju, W., Liu, C., Mu, M., Li, J., Zhou, Y., Li, X., Liu, Y., and  
1106 Chen, H.: A global 5 km monthly potential evapotranspiration dataset (1982&ndash;2015) estimated  
1107 by the Shuttleworth-Wallace model, *Earth System Science Data Discussions*, 1–45,  
1108 <https://doi.org/10.5194/essd-2023-38>, 2023.
- 1109 Tang, Q., Peterson, S., Cuenca, R. H., Hagimoto, Y., and Lettenmaier, D. P.: Satellite-based near-  
1110 real-time estimation of irrigated crop water consumption, *Journal of Geophysical Research:*  
1111 *Atmospheres*, 114, <https://doi.org/10.1029/2008JD010854>, 2009.
- 1112 Tang, R. and Li, Z.-L.: An improved constant evaporative fraction method for estimating daily  
1113 evapotranspiration from remotely sensed instantaneous observations, *Geophysical Research Letters*,  
1114 44, 2319–2326, <https://doi.org/10.1002/2017GL072621>, 2017.
- 1115 Tang, R., Li, Z.-L., Sun, X., and Bi, Y.: Temporal upscaling of instantaneous evapotranspiration on  
1116 clear-sky days using the constant reference evaporative fraction method with fixed or variable  
1117 surface resistances at two cropland sites, *Journal of Geophysical Research: Atmospheres*, 122, 784–  
1118 801, <https://doi.org/10.1002/2016JD025975>, 2017.
- 1119 Taylor, K. E.: Summarizing multiple aspects of model performance in a single diagram, *Journal of*  
1120 *Geophysical Research: Atmospheres*, 106, 7183–7192, <https://doi.org/10.1029/2000JD900719>,  
1121 2001.
- 1122 Udo; Becker, Andreas; Finger, Peter; Meyer-Christoffer, Anja; Rudolf, Bruno; Ziese, Markus: GPCP  
1123 Full Data Reanalysis Version 6.0 at 2.5°: Monthly Land-Surface Precipitation from Rain-Gauges  
1124 built on GTS-based and Historic Data., [https://doi.org/DOI:10.5676/DWD\\_GPCP/FD\\_M\\_V7\\_250](https://doi.org/DOI:10.5676/DWD_GPCP/FD_M_V7_250),  
1125 2011.
- 1126 Vermote, E: MOD09CMG MODIS/Terra Surface Reflectance Daily L3 Global 0.05Deg CMG V006  
1127 [Data set], <https://doi.org/10.5067/MODIS/MOD09CMG.006>, 2015.
- 1128 Wan, Z., Hook, S., Hulley, G: MOD11C1 MODIS/Terra Land Surface Temperature/Emissivity Daily  
1129 L3 Global 0.05Deg CMG V006 [Data set], <https://doi.org/10.5067/MODIS/MOD11C1.006>, 2015.
- 1130 Wang, K., Ma, Q., Wang, X., and Wild, M.: Urban impacts on mean and trend of surface incident  
1131 solar radiation, *Geophysical Research Letters*, 41, 4664–4668,

- 1132 <https://doi.org/10.1002/2014GL060201>, 2014.
- 1133 Wang, L., Liu, H., Chen, D., Zhang, P., Leavitt, S., Liu, Y., Fang, C., Sun, C., Cai, Q., Gui, Z., Liang,  
1134 B., Shi, L., Liu, F., Zheng, Y., and Griesinger, J.: The 1820s Marks a Shift to Hotter-Drier Summers  
1135 in Western Europe Since 1360, *Geophysical Research Letters*, 49, e2022GL099692,  
1136 <https://doi.org/10.1029/2022GL099692>, 2022.
- 1137 Wang, R., Gentine, P., Yin, J., Chen, L., Chen, J., and Li, L.: Long-term relative decline in  
1138 evapotranspiration with increasing runoff on fractional land surfaces, *Hydrology and Earth System  
1139 Sciences*, 25, 3805–3818, <https://doi.org/10.5194/hess-25-3805-2021>, 2021a.
- 1140 Wang, Y., Zhao, X., Mamtimin, A., Sayit, H., Abulizi, S., Maturdi, A., Yang, F., Huo, W., Zhou, C.,  
1141 Yang, X., and Liu, X.: Evaluation of Reanalysis Datasets for Solar Radiation with In Situ  
1142 Observations at a Location over the Gobi Region of Xinjiang, China, *Remote Sensing*, 13, 4191,  
1143 <https://doi.org/10.3390/rs13214191>, 2021b.
- 1144 White, M. A., Thornton, P. E., Running, S. W., and Nemani, R. R.: Parameterization and Sensitivity  
1145 Analysis of the BIOME–BGC Terrestrial Ecosystem Model: Net Primary Production Controls, *Earth  
1146 Interactions*, 4, 1–85, [https://doi.org/10.1175/1087-3562\(2000\)004<0003:PASAOT>2.0.CO;2](https://doi.org/10.1175/1087-3562(2000)004<0003:PASAOT>2.0.CO;2),  
1147 2000.
- 1148 Yang, D., Chen, H., and Lei, H.: Analysis of the Diurnal Pattern of Evaporative Fraction and Its  
1149 Controlling Factors over Croplands in the Northern China, *Journal of Integrative Agriculture*, 12,  
1150 1316–1329, [https://doi.org/10.1016/S2095-3119\(13\)60540-7](https://doi.org/10.1016/S2095-3119(13)60540-7), 2013.
- 1151 Yang, R. and Friedl, M. A.: Modeling the effects of three-dimensional vegetation structure on surface  
1152 radiation and energy balance in boreal forests, *Journal of Geophysical Research: Atmospheres*, 108,  
1153 <https://doi.org/10.1029/2002JD003109>, 2003.
- 1154 Zhang, C., Long, D., Zhang, Y., Anderson, M. C., Kustas, W. P., and Yang, Y.: A decadal (2008–  
1155 2017) daily evapotranspiration data set of 1 km spatial resolution and spatial completeness across  
1156 the North China Plain using TSEB and data fusion, *Remote Sensing of Environment*, 262, 112519,  
1157 <https://doi.org/10.1016/j.rse.2021.112519>, 2021.
- 1158 Zhang, K., Kimball, J. S., Mu, Q., Jones, L. A., Goetz, S. J., and Running, S. W.: Satellite based  
1159 analysis of northern ET trends and associated changes in the regional water balance from 1983 to  
1160 2005, *Journal of Hydrology*, 379, 92–110, <https://doi.org/10.1016/j.jhydrol.2009.09.047>, 2009.
- 1161 Zhang, K., Kimball, J. S., Nemani, R. R., and Running, S. W.: A continuous satellite-derived global  
1162 record of land surface evapotranspiration from 1983 to 2006, *Water Resources Research*, 46,  
1163 <https://doi.org/10.1029/2009WR008800>, 2010.
- 1164 Zhang, K., Kimball, J. S., Nemani, R. R., Running, S. W., Hong, Y., Gourley, J. J., and Yu, Z.:  
1165 Vegetation Greening and Climate Change Promote Multidecadal Rises of Global Land  
1166 Evapotranspiration, *Sci Rep*, 5, 15956, <https://doi.org/10.1038/srep15956>, 2015.
- 1167 Zhang, L., Yu, X., Zhou, T., Zhang, W., Hu, S., and Clark, R.: Understanding and Attribution of  
1168 Extreme Heat and Drought Events in 2022: Current Situation and Future Challenges, *Adv. Atmos.  
1169 Sci.*, 40, 1941–1951, <https://doi.org/10.1007/s00376-023-3171-x>, 2023a.
- 1170 Zhang, X., Huang, A., Dai, Y., Li, W., Gu, C., Yuan, H., Wei, N., Zhang, Y., Qiu, B., and Cai, S.:  
1171 Influences of 3D Sub-Grid Terrain Radiative Effect on the Performance of CoLM Over Heihe River  
1172 Basin, Tibetan Plateau, *Journal of Advances in Modeling Earth Systems*, 14, e2021MS002654,  
1173 <https://doi.org/10.1029/2021MS002654>, 2022.
- 1174 Zhang, Y.: PML\_V2 global evapotranspiration and gross primary production (2002.07-2019.08),  
1175 <https://doi.org/10.11888/Geogra.tpdc.270251>, 2022.

1176 Zhang, Y., Kong, D., Gan, R., Chiew, F. H. S., McVicar, T. R., Zhang, Q., and Yang, Y.: Coupled  
1177 estimation of 500 m and 8-day resolution global evapotranspiration and gross primary production in  
1178 2002–2017, *Remote Sensing of Environment*, 222, 165–182,  
1179 <https://doi.org/10.1016/j.rse.2018.12.031>, 2019.

1180 Zhang, Y., Li, C., Chiew, F. H. S., Post, D. A., Zhang, X., Ma, N., Tian, J., Kong, D., Leung, L. R.,  
1181 Yu, Q., Shi, J., and Liu, C.: Southern Hemisphere dominates recent decline in global water  
1182 availability, *Science*, 382, 579–584, <https://doi.org/10.1126/science.adh0716>, 2023b.

1183